XI. PLASMA ELECTRONICS*

Prof. L. D. Smullin
Prof. H. A. Haus
Prof. A. Bers
Prof. D. J. Rose
Prof. T. H. Dupree
Prof. E. P. Gyftopoulos
Dr. G. Fiocco
W. L. Brassert
H. Breindel
J. R. Cogdell
A. R. Cooke
L. J. Donadieu
W. D. Getty
B. A. Hartenbaum
G. C. Hartmann
W. C. Homeyer
H. Y. Hsieh
A. J. Impink, Jr.
P. W. Jameson
L. E. Lidsky
P. A. Mandics
D. L. Morse
A. Poeltinger
S. D. Rothleder
A. J. Schneider
P. E. Serafim
P. S. Spangler
G. C. Theodoridis
E. Thompson
J. S. Tulenko
S. Wilensky

A. ENERGY AND POWER IN MEDIA WITH TEMPORAL AND SPACIAL DISPERSION

In the last report[1] we have shown that for a linearized description of a homogeneous and time-invariant medium the time-average energy density and power density associated with the medium can be identified from a variation of Maxwell's equations with respect to both frequency and propagation vector. We shall now give a different proof of this identification of energy and power, and some illustrative examples.

Maxwell's equations for the macroscopic electric and magnetic fields in the presence of material media may be written as

$$\nabla \times \overline{E} + \mu_o \frac{\partial \overline{H}}{\partial t} = -\overline{J}_m \tag{1}$$

$$\nabla \times \overline{H} - \epsilon_o \frac{\partial \overline{E}}{\partial t} = \overline{J}_e \tag{2}$$

and Poynting's theorem has the form

$$-\nabla \cdot (\overline{E} \times \overline{H}) - \frac{\partial}{\partial t}\left(\frac{1}{2}\mu_o H^2 + \frac{1}{2}\epsilon_o E^2\right) = \overline{H} \cdot \overline{J}_m + \overline{E} \cdot \overline{J}_e. \tag{3}$$

In these equations the presence of the medium is represented by the vectors $\overline{J}_m$ and $\overline{J}_e$. In a linearized description of the medium only the first-order fields enter into Eqs. 1 and 2, and $\overline{J}_m$ and $\overline{J}_e$ are linear functions of the first-order fields. We shall consider only media for which $\overline{J}_e$ is a function of $\overline{E}$, and $\overline{J}_m$ is a function of $\overline{H}$. We Fourier analyze the fields in time and space with dependences e^{st}, $s = \nu + j\omega$, and $e^{-\overline{\gamma} \cdot \overline{r}}$, $\overline{\gamma} = \overline{\alpha} + j\overline{\beta}$, respectively. We have, in general,

* This work was supported in part by the National Science Foundation under Grant G-9330; in part by the U.S. Navy (Office of Naval Research) under Contract Nonr-1841(78); and in part by Purchase Order DDL B-00337 with Lincoln Laboratory, a center for research operated by Massachusetts Institute of Technology with the joint support of the U. S. Army, Navy, and Air Force under Air Force Contract AF 19(604)-7400.

$$\bar{J}_m = s\mu_o \bar{\bar{\chi}}_m(\bar{\gamma}, s) \cdot \bar{H} \tag{4}$$

$$\bar{J}_e = s\epsilon_o \bar{\bar{\chi}}_e(\bar{\gamma}, s) \cdot \bar{E} \tag{5}$$

Here, the susceptibility tensors $\bar{\bar{\chi}}_m$ and $\bar{\bar{\chi}}_e$ are obtained from the linearized description of the interaction between the medium and the electromagnetic fields. In the steady state the Fourier components may be chosen with time dependence $e^{j\omega t}$ and the susceptibility tensors become $\bar{\bar{\chi}}_m(\bar{\gamma},\omega)$ and $\bar{\bar{\chi}}_e(\bar{\gamma},\omega)$. The time average of Eq. 3 gives

$$2\bar{\alpha} \cdot \left(\mathrm{Re}\tfrac{1}{2}\bar{E}\times\bar{H}^*\right) = \tfrac{1}{2}\mathrm{Re}\left(\bar{H}\cdot\bar{J}_m^* + \bar{E}\cdot\bar{J}_e^*\right)$$

$$= \tfrac{1}{2}\omega\left[\mu_o\bar{H}^* \cdot j\bar{\bar{\chi}}_m^a \cdot \bar{H} + \epsilon_o\bar{E}^* \cdot j\bar{\bar{\chi}}_e^a \cdot \bar{E}\right] \tag{6}$$

where $\bar{\bar{\chi}}_m^a$ and $\bar{\bar{\chi}}_e^a$ are the anti-Hermitian parts of $\bar{\bar{\chi}}_m(\bar{\gamma},\omega)$ and $\bar{\bar{\chi}}_e(\bar{\gamma},\omega)$, respectively. If $j\bar{\bar{\chi}}_m^a$ and $j\bar{\bar{\chi}}_e^a$ are positive definite, the right-hand side of Eq. 6 represents the time-average power density loss, and the medium is passive. If either $j\bar{\bar{\chi}}_m^a$ or $j\bar{\bar{\chi}}_e^a$ is negative definite, the medium is active in the sense that time-average electromagnetic power is being generated. If $j\bar{\bar{\chi}}_m^a$ and $j\bar{\bar{\chi}}_e^a$ are zero, the medium is "lossless." However, potentially, it may still be either active or passive (or even unstable), the choice depending upon its energy state.

The energy and power in a lossless medium can be determined as follows. In the absence of loss the Fourier components of the fields may be chosen with time dependence $e^{j\omega t}$ and $e^{-j\bar{\beta}\cdot\bar{r}}$, and the medium tensors are $\bar{\bar{\chi}}_m(\bar{\beta},\omega)$ and $\bar{\bar{\chi}}_e(\bar{\beta},\omega)$. Consider a very slightly lossy medium, and let the Fourier space components be $e^{-\bar{\gamma}\cdot\bar{r}}$, with

$$|\bar{\alpha}| \ll |\bar{\beta}| \tag{7}$$

and assume that the electromagnetic fields are driven with time dependence e^{st} and that

$$\nu \ll \omega. \tag{8}$$

Maxwell's equations, Eqs. 1 and 2, become

$$\bar{\gamma}\times\bar{E} - s\,\mu_o\bar{H} = s\,\mu_o\bar{\bar{\chi}}_m \cdot \bar{H} \tag{9}$$

$$\bar{\gamma}\times\bar{H} + s\,\epsilon_o\bar{E} = -\,s\,\epsilon_o\bar{\bar{\chi}}_e \cdot \bar{E} \tag{10}$$

Dot-multiplying Eq. 9 by $\bar{H}^*$ and the complex conjugate of Eq. 10 by $-\bar{E}$, adding the resultant equations, and taking the real part, we obtain

$$2\bar{\alpha} \cdot \left(\mathrm{Re}\tfrac{1}{2}\bar{E}\times\bar{H}^*\right) - 2\nu\left(\tfrac{1}{4}\mu_o|\bar{H}|^2 + \tfrac{1}{4}\epsilon_o|\bar{E}|^2\right)$$

$$= \tfrac{1}{2}\mathrm{Re}\left[s\,\mu_o\,\bar{H}^* \cdot \bar{\bar{\chi}}_m \cdot \bar{H} + s^*\epsilon_o\bar{E}\cdot\bar{\bar{\chi}}_e\cdot\bar{E}^*\right] \tag{11}$$

Under the condition of Eq. 8, the time-average electromagnetic power flow can be identified with $2\bar{\alpha}\cdot\left(\mathrm{Re}\tfrac{1}{2}\bar{E}\times\bar{H}^*\right)$ as in Eq. 6. With the assertions of very small loss, and Eqs. 7 and 8, we evaluate the right-hand side of Eq. 11 to first order in both ν and α. Thus

$$\bar{\bar{\chi}}(\bar{\gamma},\omega) = \bar{\bar{\chi}}(\bar{\beta},\omega) + \frac{\partial\bar{\bar{\chi}}}{\partial\omega}(-j\nu) + \frac{\partial\bar{\chi}}{\partial\bar{\beta}}\cdot(-j\bar{\alpha}). \tag{12}$$

Then, substituting Eq. 12 in Eq. 11, we obtain

$$2\bar{\alpha}\cdot(\bar{p}_e+\bar{p}_M) = 2\nu\left[w_m+w_e+w_M\right] + \bar{p}_d, \tag{13}$$

where

$$\bar{p}_e = \mathrm{Re}\,\tfrac{1}{2}\bar{E}\times\bar{H}^* \tag{14}$$

$$w_m = \tfrac{1}{4}\mu_o|\bar{H}|^2 \tag{15}$$

$$w_e = \tfrac{1}{4}\epsilon_o|\bar{E}|^2 \tag{16}$$

$$\bar{p}_M = -\tfrac{1}{4}\mu_o\bar{H}^*\cdot\frac{\partial\left(\omega\bar{\bar{\chi}}_m^h\right)}{\partial\bar{\beta}}\cdot\bar{H} - \tfrac{1}{4}\epsilon_o\bar{E}^*\cdot\frac{\partial\left(\omega\bar{\bar{\chi}}_e^h\right)}{\partial\bar{\beta}}\cdot\bar{E} \tag{17}$$

$$w_M = \tfrac{1}{4}\mu_o\bar{H}^*\cdot\frac{\partial\left(\omega\bar{\bar{\chi}}_m^h\right)}{\partial\omega}\cdot\bar{H} + \tfrac{1}{4}\epsilon_o\bar{E}^*\cdot\frac{\partial\left(\omega\bar{\bar{\chi}}_e^h\right)}{\partial\omega}\cdot\bar{E} \tag{18}$$

$$\bar{p}_d = \tfrac{1}{2}\omega\left[\mu_o\bar{H}^*\cdot j\bar{\bar{\chi}}_m^a\cdot\bar{H} + \epsilon_o\bar{E}^*\cdot j\bar{\bar{\chi}}_e^a\cdot\bar{E}\right], \tag{19}$$

where $\bar{\bar{\chi}}_m^h$ and $\bar{\bar{\chi}}_e^h$ are the Hermitian parts of $\bar{\bar{\chi}}_m$ and $\bar{\bar{\chi}}_e$. Equation 13 expresses the conservation of energy to first order in the quantities $\bar{\bar{\chi}}_m^a$, $\bar{\bar{\chi}}_e^a$, ν, and α. The last term is readily identified with the time-average power density in the first-order loss $\bar{\bar{\chi}}_m^a$ and $\bar{\bar{\chi}}_e^a$. It also follows that w_M and $\bar{p}_M$ must be associated with the time-average energy density and power density, respectively, of the medium.

The group velocity is found as before,[1] and equals the energy velocity,

$$\frac{\partial\omega}{\partial\bar{\beta}} = \frac{\bar{p}_e+\bar{p}_M}{w_m+w_e+w_M}. \tag{20}$$

We shall now illustrate our results with two very simple and well-known examples.

(XI. PLASMA ELECTRONICS)

1. One-Dimensional Warm Plasma

Consider a lossless stationary plasma having an equilibrium temperature T, and with only the longitudinal wave of interest. From the linearized force equation and continuity equation the first-order current density and electric field are related by

$$J = -j\omega\epsilon_o \frac{\omega_p^2}{\left(\omega^2 - v_T^2\beta^2\right)} E, \tag{21}$$

where

$$v_T^2 = \frac{\gamma kT}{m} \tag{22}$$

is the mean-square velocity fluctuation. With the susceptibility of Eq. 21 in Eqs. 17 and 18, we obtain

$$p_M = \frac{1}{4}\epsilon_o |E|^2 \frac{2\beta v_T^2 \omega_p^2}{\left(\omega^2 - v_T^2\beta^2\right)^2} \tag{23}$$

$$w_M = \frac{1}{4}\epsilon_o |E|^2 \frac{\omega_p^2\left(\omega^2 + v_T^2\beta^2\right)}{\left(\omega^2 - v_T^2\beta^2\right)^2}. \tag{24}$$

For any real value of β the time-average energy density is positive. Hence these waves are passive. The dispersion equation for these waves is

$$\beta = \pm \frac{\sqrt{\omega^2 - \omega_p^2}}{v_T}. \tag{25}$$

Using Eq. 25 in Eqs. 23, 24, and 21, we obtain

$$p_M = \frac{1}{4}\epsilon_o |E|^2 \, 2\beta \frac{v_T^2}{\omega_p^2} \tag{26}$$

$$w_M = \frac{1}{4}\epsilon_o |E|^2 \left(2\frac{\omega^2}{\omega_p^2} - 1\right) \tag{27}$$

$$\frac{\partial\omega}{\partial\beta} = \frac{p_M}{w_e + w_M} = \frac{\beta}{\omega} v_T^2. \tag{28}$$

Equation 26 gives the time-average acoustic power density, and Eq. 27 gives the time-average kinetic and poteneial energies associated with these waves.

2. One-Dimensional Electron Beam

Consider a lossless, cold, electron beam having an unperturbed velocity v_o, and look for the longitudinal waves. The linearized force equation and continuity give

$$J = -j\omega\epsilon_o \frac{\omega_p^2}{(\omega - v_o\beta)^2} E, \tag{29}$$

where E and J are in the direction of v_o. Equations 17 and 18 then give

$$p_M = \frac{1}{4}\epsilon_o |E|^2 \frac{2\omega v_o \omega_p^2}{(\omega - v_o\beta)^3} \tag{30}$$

$$w_M = \frac{1}{4}\epsilon_o |E|^2 \frac{\omega_p^2(\omega + v_o\beta)}{(\omega - v_o\beta)^3}. \tag{31}$$

Equation 31 shows that for real values of $\beta > \omega/v_o$ the time-average energy density associated with the medium is negative, and hence such waves may be active. The dispersion equation for the waves is

$$\beta = \frac{\omega \mp \omega_p}{v_o} \tag{32}$$

which gives the fast and slow space-charge waves. Hence the slow space-charge wave may be active. Using Eq. 32 in Eqs. 30, 31, and 20, we find that

$$p_M = \frac{1}{4}\epsilon_o |E|^2 \frac{2\omega v_o}{(\pm\omega_p)} \tag{33}$$

$$w_M = \frac{1}{4}\epsilon_o |E|^2 \frac{(2\omega \mp \omega_p)}{(\pm\omega_p)} \tag{34}$$

$$w_M + w_e = \frac{1}{4}\epsilon_o |E|^2 \frac{2\omega}{(\pm\omega_p)} \tag{35}$$

$$\frac{\partial\omega}{\partial\beta} = v_o. \tag{36}$$

Equation 25 shows that the fast space-charge wave is passive, and the slow space-charge

wave is active. They carry positive and negative kinetic power that is given by Eq. 33 in the direction of the unperturbed velocity v_o given by Eq. 36.

A. Bers

References

1. A. Bers, Properties of waves in time- and space-dispersive media, Quarterly Progress Report No. 65, Research Laboratory of Electronics, M.I.T., April 15, 1962, pp. 89-93.

B. ELECTRON BEAM-PLASMA INTERACTION EXPERIMENTS

The study of plasma heating by the electron beam-plasma interaction has continued with emphasis on the use of long beam pulses and a magnetic-mirror confining field. The oscillations are initiated by the interaction between the electron beam and the plasma generated by ionizing collisions of beam electrons and residual gas atoms. The initial interaction, which was discussed in a previous report,[1] takes place within a few microseconds and results in a considerable increase in the rate of plasma production above that caused by the unperturbed electron beam. We believe that the large increase in ionization results in a change from the initial (cyclotron) oscillation mode to a second mode, whose most prominent characteristic is that the expected frequency of oscillation is near the plasma resonance frequency. This mode would be expected to play a dominant role in the interaction, as higher plasma densities are reached during longer beam pulses.

An increase in the beam pulse length from a few microseconds to the range 20-300 μsec has resulted in a more intense interaction in many respects. By adjusting the operating conditions, we can produce initial effects in the first few microseconds of the pulse which are similar to those observed with short pulses.[1] As the beam current continues to flow, however, it appears that the second mode becomes dominant for periods as long as 300 μsec. During this time, X-rays are produced at energies well above the dc beam energy, and a large ionization rate is evidenced by changes in the electrode currents. This report will present preliminary measurements and observations of these phenomena. The experiments were made with two systems, which will be identified by letters A and B. System A has been described previously,[1] and System B will be described in this report.

1. Operation with Long Pulses in System A

In System A, electron-beam pulses of from 20 μsec to 200 μsec duration were used to investigate the beam-plasma interaction. The plasma is created by beam ionization of the background gas, which is argon or hydrogen. The operating pressures are varied

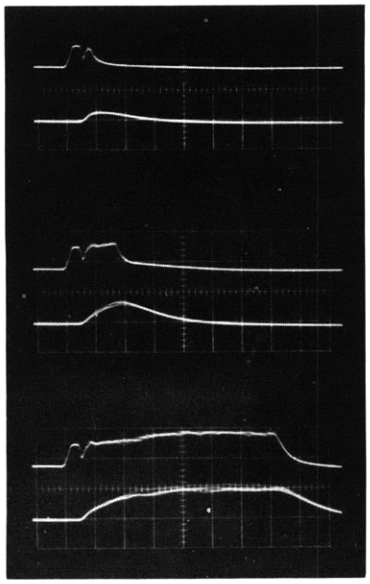

Fig. XI-1. System A. (Argon sweep rate = 5 μsec/cm; beam voltage = 5 kv; current calibration = 1 amp/cm.) Collector current I_c (upper trace) and light intensity (lower trace) for varying beam pulse lengths. The break in the current occurs approximately 3 μsec after the initial rise of current. The value of current before the break is the "vacuum" value, that is, the collector current at low pressures when no oscillations are present.

from 10^{-4} mm Hg to 10^{-3} mm Hg. The confining magnetic field is mirror-shaped, with a mirror ratio of 1.6. The induction in the central portion of the mirror field is varied from 100 gauss to 1000 gauss.

The accompanying photographs are examples of our general observations. Figure XI-1 shows the early breakup of the beam, which is very much like that observed in the short-pulse studies.[1] The breakup is more noticeable at low magnetic field strengths. Figure XI-1 and, to a lesser degree, Fig. XI-2 illustrate the increased collector current, which sometimes increases to twice the value of the "vacuum" collector current. This increase is best illustrated by the third trace in Fig. XI-1. The wall current, defined as the difference between the input gun cathode current and the collector current, exhibits the usual electron flow at the time of beam breakup.[1] Its behavior at later times, however, depends on the type of gas used. With argon, the wall current changes sign, indicating ion flow to the walls, in accompaniment with an increased electron flow to the collector. With hydrogen, Fig. XI-2a, there is no observable ion flow to the walls and little increase in the collector electron current. Figures XI-2b, XI-3, and XI-4 illustrate the bursts of X-rays detected with a polyvinyl plastic scintillator and photomultiplier. The scintillation detector output generally decreases when the collector current

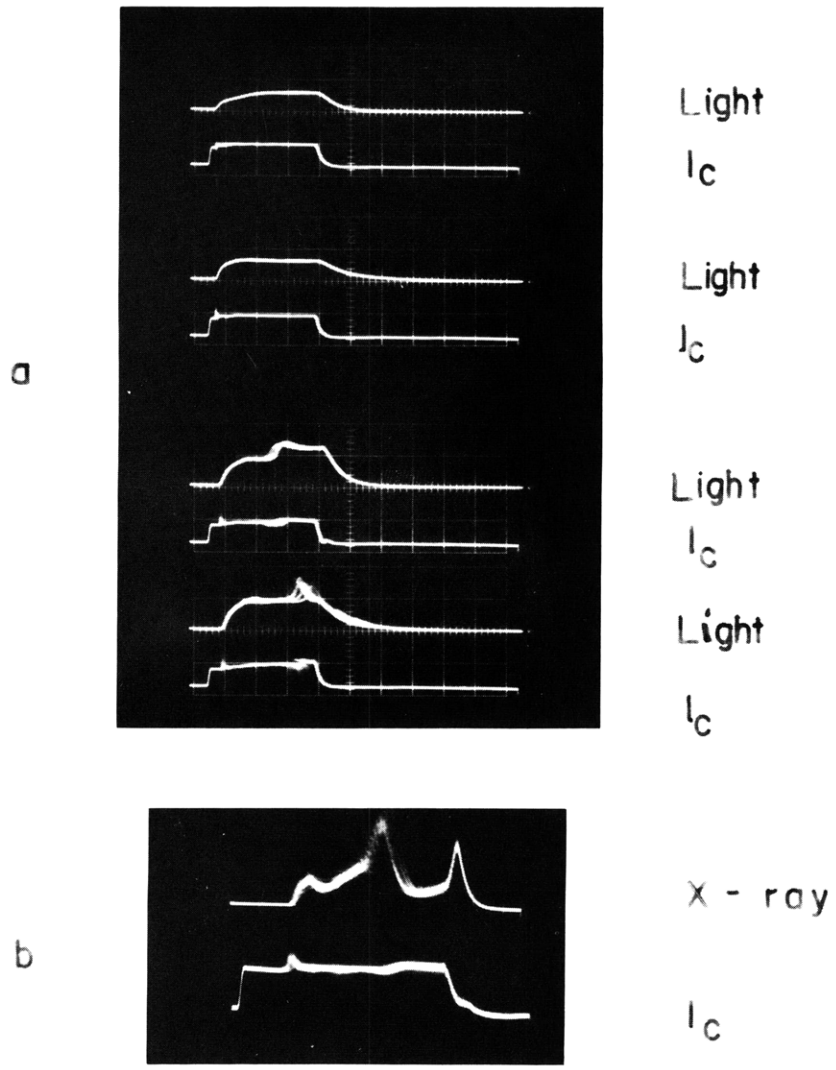

Fig. XI-2. System A. (Hydrogen sweep rate = 10 μsec/cm; beam voltage = 10 kv; current calibration = 1 amp/cm.) (a) Behavior of the light and collector current pulses in hydrogen. The minimum magnetic induction along the beam path varies from 120 gauss in the top trace to 500 gauss in the lower trace. (b) X-ray indication by a plastic scintillator for conditions of third trace in part (a).

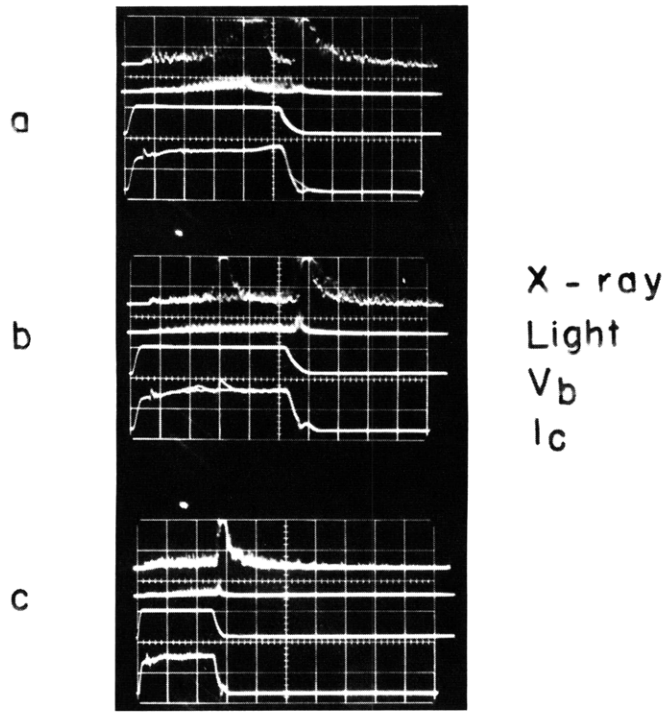

Fig. XI-3. System A. (Hydrogen sweep rate = 10 μsec/cm; beam voltage = 10 kv; current calibration = 1 amp/cm.) X-ray, light-beam voltage (V_b) and collector current (I_c) oscillograms for varying magnetic induction: (a) 670 gauss, (b) 823 gauss, (c) 1060 gauss. These oscillograms illustrate that X-rays persist long after the beam is turned off.

and light output increase, as shown by Fig. XI-2b. The X-ray intensity persists for long periods after the beam pulse is turned off, as shown in Fig. XI-3. Low-frequency modulations of the X-ray intensity are also observed, as illustrated in Fig. XI-4.

A preliminary absorption experiment was performed to estimate the energy of the X-rays. Several sheets of aluminum with thicknesses varying from 0.030 in. to 0.250 in. were interposed between the Plexiglas viewing port of System A and the scintillation detector. The relative intensities of the X-rays detected for different aluminum sheets were measured. If we assume that

(a) the oscilloscope display of the scintillation detector output is directly proportional to the energy of the X-rays, and

(b) the X-rays are confined to a "narrow beam" of monochromatic wavelength,

then relative intensity measurements yield the absorption coefficient, which can be used to estimate the unknown X-ray wavelength. The slope of the semi-log plot of relative intensity versus shielding thickness of aluminum gives a mass absorption coefficient of $\mu/\rho = 2.0\ \text{cm}^2/\text{gm}$. This corresponds approximately to an X-ray wavelength of 0.497 Å,

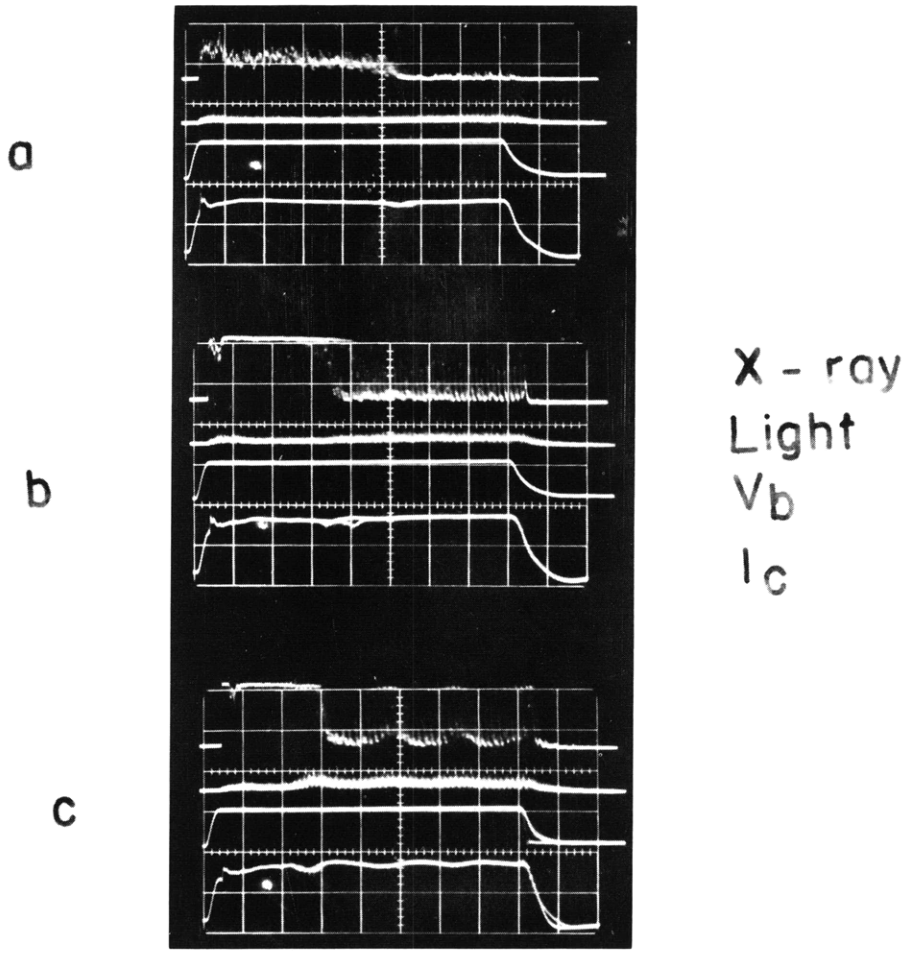

Fig. XI-4. A set of oscillograms similar to those of Fig. XI-3, taken at lower magnetic induction (in the range 250-350 gauss). The traces in sets (b) and (c) illustrate low-frequency modulations of the X-ray intensity.

or to an energy of 25 kev. This result is interesting because 0.497 Å corresponds to the wavelength of the K_α emission lines of tin, which is present in the bronze wall of the vacuum chamber and in the solder coating on this wall.

Two other properties of the X-rays which are important and deserve some comment are the "afterglow" tail shown in Fig. XI-3 and the low-frequency modulations of intensity illustrated in Fig. XI-4. The long decay of the X-ray intensity was found at many operating conditions when a weak mirror field was formed. Roughly, exponential decays with time constants as long as 80-120 μsec were observed.

The low-frequency oscillations may be indicative of excitation of ion oscillations. The frequency of the oscillations such as these shown in Fig. XI-4 is apparently unrelated to the magnetic field. The source of these oscillations will be sought in future work.

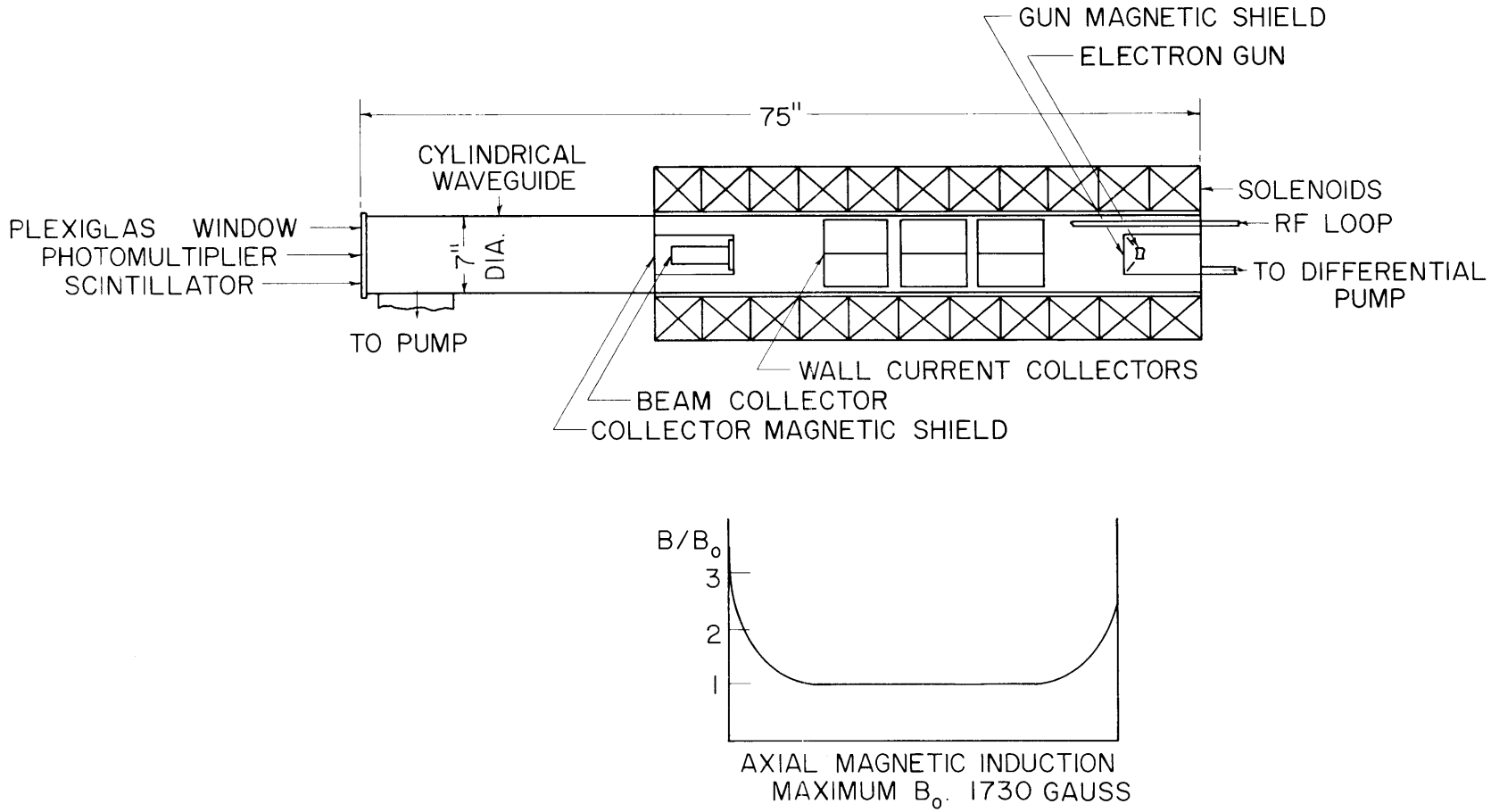

SCHEMATIC OF SYSTEM B

Fig. XI-5. Schematic diagram of System B.

The beam pulse length that was necessary for producing all of the phenomena summarized in Figs. XI-1 to XI-4 is, at most, 200 μsec. Experiments with longer pulses revealed no changes in the general behavior.

2. Operation with System B

A system considerably larger than System A has been constructed for further study of beam-plasma interactions. The main features of System B, which is shown schematically in Fig. XI-5, are:

(i) A stainless-steel tube 7 inches in diameter and 75 inches long.

(ii) A magnetic-field system composed of: (a) a solenoid that extends along 49 inches of the waveguide; (b) iron pole pieces that produce a mirror field with a ratio of approximately 3.2 to 1; and (c) a maximum "uniform" field of 1730 gauss extending for 23 inches along the beam path.

(iii) A magnetically shielded electron gun of perveance 10^{-6} (1 amp at 10 kv).

(iv) A vacuum system capable of producing a base pressure of less than 10^{-6} mm Hg.

(v) A pulser that produces up to 12-kv pulses that may be as long as several hundred microseconds with a variable repetition rate.

(vi) Provision for measuring beam collector current, rf fields, X-ray intensity, light, and currents that cross the magnetic field to reach the wall of the stainless-steel tube.

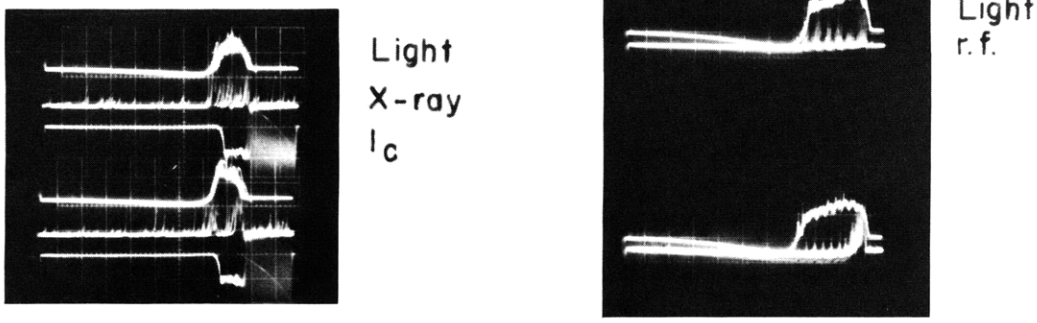

Fig. XI-6. System B. (Hydrogen sweep rate = 50 μsec/cm; beam voltage = 11.4 kv; pressure = 0.15 μ Hg. Time runs from right to left. Current calibration = 1 amp/cm.) (a) Light, X-ray and collector current oscillograms. Magnetic induction (B_o): 324 gauss in upper set, 540 gauss in lower set. (b) Light and rf envelope. Magnetic induction (B_o) : 486 gauss in upper set and 324 gauss in lower set. RF frequency: 13.4 kmc in upper set and 12.7 kmc in lower set.

In preliminary experiments we have observed the collector current, X-rays, light, and rf fields. Oscillograms are shown in Fig. XI-6. The experiments were run at pressures between 1.5×10^{-4} and 3×10^{-4} mm Hg in hydrogen gas. At higher pressures gun cathode emission was reduced. This limitation will be corrected by differential pumping of the gun chamber.

The collector current is characterized by two types of oscillations. A large-amplitude, 10-mc oscillation begins as soon as beam current is collected. The current oscillates between +1 (ions) and −2 (electrons) amps, for example, when the dc collector current is −1 ampere. These oscillations may last for 100 μsec. As the pulse length is increased beyond 100 μsec, the 10-mc oscillations suddenly stop and are followed by a low-frequency, low-amplitude fluctuation. Typically, the current varies ±10 per cent at frequencies of approximately 100 kc. This fluctuation continues until the end of the pulse. An example of both types of behavior is shown in Fig. XI-6a. Coincident with the beginning of the low-frequency collector-current fluctuation is the production of light and X-rays, as shown in Fig. XI-6a. Large, pulsating bursts of light and rf are shown in Fig. XI-6b. The X-rays may continue after the beam pulse has ended, but the light and rf do not. The rf frequency in Fig. XI-6b is 14.3 kmc. Assuming that this frequency is the plasma resonance frequency, under the assumption that a strong interaction is predicted at this frequency, a density of 2.5×10^{12} electrons/cm^3 is indicated. In these experiments the light attributable to the plasma is visible out to the walls of the stainless-steel tube. Insulated collector electrodes are being placed near the wall in order to determine the nature of the currents arriving there. In particular, we are interested in observing whether or not any low-frequency, higher-order angular modes can be detected.

L. D. Smullin, W. D. Getty, B. A. Hartenbaum, H. Y. Hsieh

References

1. L. D. Smullin and W. D. Getty, Large-signal electron-stimulated plasma oscillations, Quarterly Progress Report No. 64, Research Laboratory of Electronics, M.I.T., January 15, 1962, pp. 113-117.

C. A MAGNETOHYDRODYNAMIC SMALL-SIGNAL POWER THEOREM

A small-signal power theorem will be derived that is useful in the study of a magnetohydrodynamic active waveguide problem.

We consider a case in which a fluid flows colinearly with a uniform dc magnetic field. Ignoring the electric displacement current, we find that the appropriate linearized equations of the system are:

Maxwell's equations

$$\nabla \times \overline{H} = \overline{J} \tag{1}$$

$$\nabla \times \overline{E} = -\frac{\partial \mu_o \overline{H}}{\partial t}, \tag{2}$$

Ohm's law

$$J = \sigma (\overline{E} + \overline{v} \times \overline{B}_o + \overline{v}_o \times \overline{B}), \tag{3}$$

The momentum equation

$$\rho_o \frac{D}{Dt} \overline{v} + \nabla p = \overline{J} \times \overline{B}_o, \tag{4}$$

The conservation of matter equation

$$\frac{D}{Dt} \rho = -\rho_o (\nabla \cdot \overline{v}), \tag{5}$$

The equation of state

$$p = c_s^2 \rho, \tag{6}$$

where $\frac{D}{Dt} = \frac{\partial}{\partial t} + \overline{v}_o \cdot \nabla$. Variables with a subscript zero represent dc quantities; variables without subscripts represent small-signal quantities.

Stating Poynting's theorem in the usual manner, we have

$$\nabla \cdot (\overline{E} \times \overline{H}) + \frac{\partial}{\partial t} \mu_o \frac{\overline{H} \cdot \overline{H}}{2} + \overline{E} \cdot \overline{J} = 0. \tag{7}$$

The $\overline{E} \cdot \overline{J}$ term indicates that electromagnetic energy is not conserved. How much of the unconserved electromagnetic energy is transferred to mechanical and thermodynamic forms of energy and how much of it is dissipated in ohmic losses can be determined by the evaluation of the $\overline{E} \cdot \overline{J}$ term through the remaining equations. The algebraic procedure involved in the transformation is rather complicated and will be summarized here.

If the vector product of Eq. 3 and $\overline{B}_o$ is combined with Eq. 4 in a scalar product, the result is

$$\overline{E} \cdot \overline{J} = \left(\overline{v}_t - \frac{v_o}{B_o} \overline{B}_t \right) \cdot \left(\rho_o \frac{D}{Dt} \overline{v} + \nabla p \right) + \frac{\overline{J} \cdot \overline{J}}{\sigma}, \tag{8}$$

where the subscript t represents the portion of the vector which is transverse to the magnetic field. Through the use of Eqs. 2-6, Eq. 8 can be transformed.

$$\overline{E}\cdot\overline{J}=\frac{\partial}{\partial t}\left[\frac{1}{2}\rho_o\overline{v}\cdot\overline{v}+(\overline{v}_o\cdot\overline{v})\rho+\frac{p\rho}{2\rho_o}-\frac{v_o}{B_o}\overline{B}\cdot\overline{v}\right]+\nabla$$

$$\cdot\left\{p\overline{v}-\frac{v_o}{B_o}p\overline{B}+\overline{v}_o\left[\rho_o\overline{v}\cdot\overline{v}+\rho(\overline{v}_o\cdot\overline{v})+\frac{p\rho}{\rho_o}-\frac{v_o}{B_o}\overline{B}\cdot\overline{v}\right]\right\}+\frac{\overline{J}\cdot\overline{J}}{\sigma}. \tag{9}$$

When this expression is substituted in Eq. 7, the result is

$$\nabla\cdot(\overline{E}\times\overline{H}+\overline{S}_K)+\frac{\partial}{\partial t}(w_m+w_k)+\frac{\overline{J}\cdot\overline{J}}{\sigma}=0, \tag{10}$$

where

$$\overline{S}_K=p\overline{v}-\frac{v_o}{B_o}p\overline{B}+\overline{v}_o\left[\rho_o\overline{v}\cdot\overline{v}+\rho(\overline{v}_o\cdot\overline{v})+\frac{p\rho}{\rho_o}-\frac{v_o}{B_o}\overline{B}\cdot\overline{v}\right]$$

$$w_m=\frac{1}{2\mu_o}\overline{B}\cdot\overline{B}$$

and

$$w_k=\frac{1}{2}\rho_o\overline{v}\cdot\overline{v}+(\overline{v}_o\cdot\overline{v})\rho+\frac{p\rho}{2\rho_o}-\frac{v_o}{B_o}\overline{B}\cdot\overline{v}.$$

In the limit of infinite conductivity, Eq. 10 takes the form of a conservation principle, expressing the fact that the time rate of change of a "stored energy" density integrated over a volume is the same thing as an integration of a "power flux" over the surface of the volume.

Our use of Eq. 10 for a fluid interacting with an external circuit requires an examination of its validity at a fluid-vacuum interface. We shall show that the power flux term is continuous across the fluid surface. (See Fig. XI-7.)

The requirement for continuity of the power flux is

$$(\overline{E}^{(1)}\times\overline{H}^{(1)}+\overline{S}_K)\cdot\overline{n}=\overline{E}^{(2)}\times\overline{H}^{(2)}\cdot\overline{n}, \tag{11}$$

where

$$\overline{S}_K\cdot\overline{n}=p\left(\overline{v}^{(1)}-\frac{v_o}{B_o}\overline{B}^{(1)}\right)\cdot\overline{n}, \tag{12}$$

since $\overline{n}$ is a transverse vector. The validity of Eq. 11 is established by the boundary conditions. A force balance at the fluid surface requires

$$p^{(1)}+\overline{B}_o^{(1)}\cdot\overline{H}^{(1)}=\overline{B}_o^{(2)}\cdot\overline{H}^{(2)}. \tag{13}$$

The fact that the fluid is a perfect conductor requires that no total magnetic flux cross

the fluid surface; this requirement can be expressed as

$$\frac{\bar{B}^{(1)} \cdot \bar{n}}{B_o^{(1)}} = \frac{\bar{B}^{(2)} \cdot \bar{n}}{B_o^{(2)}} . \tag{14}$$

The requirement that the electric field transverse to the interface be continuous in a frame of reference moving coincidentally with the interface transforms into the stationary frame of reference:

$$\bar{N} \times \left[\bar{E}^{(2)} + \bar{v}_o \times \bar{B}^{(2)} + \bar{v} \times \bar{B}_o^{(2)} \right] = \bar{N} \times \left[\bar{E}^{(1)} + \bar{v}_o \times \bar{B}^{(1)} + \bar{v} \times \bar{B}_o^{(1)} \right] \tag{15}$$

Using Ohm's law in the limit of infinite conductivity, we find that

$$\left(\bar{E}^{(1)} \times \bar{H}^{(1)} + \bar{S}_K \right) \cdot \bar{n} = \left(p + \bar{B}_o^{(1)} \cdot \bar{H}^{(1)} \right) \left(\bar{v} - \frac{v_o}{B_o^{(1)}} \bar{B}^{(1)} \right) \cdot \bar{n};$$

and using boundary condition (15) and Ohm's law, we find that

$$\bar{E}^{(2)} \times \bar{H}^{(2)} \cdot \bar{n} = \left(\bar{B}_o^{(2)} \cdot \bar{H}^{(2)} \right) \left(\bar{v} - \frac{v_o}{B_o^{(2)}} \bar{B}^{(2)} \right) \cdot \bar{n}$$

which, when considered in conjunction with the other boundary conditions, establishes the validity of Eq. 11.

We can integrate Eq. 10 over a volume through which the beam passes. (See Fig. XI-8.) Using Gauss' theorem, we obtain

$$\int_{\text{total surface}} \bar{E} \times \bar{H} \cdot ds + \int_{S_1+S_2} \bar{S}_K \cdot d\bar{s} + \frac{\partial}{\partial t} \int_{\text{total volume}} w_m \, dv + \frac{\partial}{\partial t} \int_{\text{beam volume}} w_K \, dv = 0 \tag{16}$$

In harmonic solutions, the time average of the last two terms of Eq. 16 vanishes and we find that, to obtain time-average electromagnetic energy from the volume, the kinetic power term must decrease from the entrance to the exit of the volume.

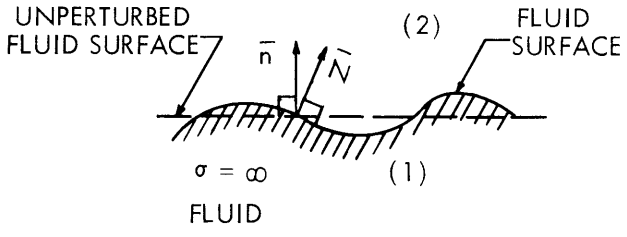

Fig. XI-7. Perturbed fluid surface.

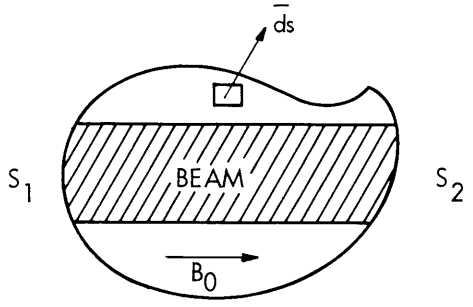

Fig. XI-8. Integration volume.

J. R. Cogdell

References

1. H. A. Haus, Electron-Beam Waves in Microwave Tubes, Technical Report 316, Research Laboratory of Electronics, M.I.T., April 8, 1958, page 99.

D. MAGNETOHYDRODYNAMIC GENERALIZATION OF KELVIN'S THEOREM

A generalization of Kelvin's theorem to the magnetohydrodynamic case has been carried out using the magnetohydrodynamic equations of motion. A similar theorem was derived from a Hamiltonian formulation by P. Penfield[1] and, in fact, his theorem suggested the present approach. Because the Lin variables and certain Lagrange multipliers do not appear in the present theorem, it may prove to be more directly applicable to specific physical problems. The equations of magnetohydrodynamics are:

The force equation

$$\frac{d}{dt}\bar{v} = \frac{\partial \bar{v}}{\partial t} + \bar{v} \cdot \nabla \bar{v} = -\frac{\nabla p}{\rho} + \frac{\bar{J} \times \bar{B}}{\rho} \tag{1}$$

Ampere's law

$$\nabla \times \bar{B} = \mu_o \bar{J} \tag{2}$$

The continuity equation

$$\frac{d}{dt}\rho = -\rho \nabla \cdot \bar{v} \tag{3}$$

The equation of state

$$p = p(\rho) \tag{4}$$

Ohm's law for a perfectly conducting fluid

$$\bar{E} + \bar{v} \times \bar{B} = 0 \tag{5}$$

Faraday's law

$$\nabla \times \bar{E} = -\frac{\partial \bar{B}}{\partial t}. \tag{6}$$

Combining Eqs. 3, 5, and 6, we obtain Walén's theorem which is convenient for our purpose

$$\frac{d}{dt}\left(\frac{\bar{B}}{\rho}\right) = \frac{\bar{B}}{\rho} \cdot \nabla \bar{v}. \tag{7}$$

In order to generalize Kelvin's theorem, it is necessary to introduce a quantity akin to the vector potential that is used to prove the conservation of the generalized momentum in classical electrodynamics. This quantity has arisen in Penfield's work,[1] and is

related to the current density as

$$\bar{J} = \frac{\partial \bar{\bar{\pi}}}{\partial t} + \nabla \times (\bar{\bar{\pi}} \times \bar{v}). \tag{8}$$

The divergence of $\bar{\bar{\pi}}$ is chosen:

$$\nabla \cdot \bar{\bar{\pi}} = 0, \tag{9}$$

so that the divergence-free character of $\bar{J}$ is ensured. Note that the relation between $\bar{\bar{\pi}}$ and $\bar{J}$ is the same as the one relating the current density and polarization for moving polarized media.[2] Whereas a stationary polarized material cannot support a dc current, the present situation may allow for one if $\bar{\bar{\pi}}$ grows linearly with time.

For any physical current distribution, $\bar{J}(\bar{r}, t)$, $\bar{\bar{\pi}}$ is not determined uniquely by (8) and (9). In order to check the extent to which two different space-time functions $\bar{\bar{\pi}}_1$ and $\bar{\bar{\pi}}_2$ may describe the same current density distribution $\bar{J}(\bar{r}, t)$, we define their difference

$$\bar{\bar{\pi}}_d = \bar{\bar{\pi}}_1 - \bar{\bar{\pi}}_2. \tag{10}$$

It follows from Eqs. 8 and 9 that

$$\nabla \cdot \bar{\bar{\pi}}_d = 0 \tag{11}$$

and

$$\frac{\partial \bar{\bar{\pi}}_d}{\partial t} + \nabla \times (\bar{\bar{\pi}}_d \times \bar{v}) = 0. \tag{12}$$

Accordingly, $\bar{\bar{\pi}}_d$ satisfies the equation

$$\frac{d}{dt} \int \bar{\bar{\pi}}_d \cdot d\bar{a} = 0 \tag{13}$$

for any surface imbedded in the fluid and traveling with the fluid. If we set $\bar{\bar{\pi}}_1 = \bar{\bar{\pi}}_2 = 0$, at $t = 0$, it follows that $\bar{\bar{\pi}}_d = 0$ at $t = 0$. From Eq. 12 we conclude that $\bar{\bar{\pi}}_d$ has to stay zero at all times and therefore the additional requirement

$$\bar{\bar{\pi}} = 0; \quad t = 0 \tag{14}$$

is sufficient to specify $\bar{\bar{\pi}}$ uniquely.

We turn to the derivation of the generalized Kelvin theorem. We use the vector identity

$$\bar{v} \cdot \nabla \bar{v} = \frac{1}{2} \nabla v^2 - \bar{v} \times (\nabla \times \bar{v}) . \tag{15}$$

Furthermore, if the pressure is a function of the density alone, or vice versa, $\rho = \rho(p)$. $\nabla p/\rho$ may be written as the gradient of a scalar function. Using (7) and (8), we can show that the magnetic force density can be written in the form[3]

$$\frac{\bar{J}\times\bar{B}}{\rho} = \frac{\partial}{\partial t}\left(\frac{\bar{\pi}\times\bar{B}}{\rho}\right) - \nabla\left(\frac{\bar{\pi}\cdot\bar{v}\times\bar{B}}{\rho}\right) - \bar{v}\times\left(\nabla\times\frac{\bar{\pi}\times\bar{B}}{\rho}\right) . \tag{16}$$

Introducing (15) and (16) into Eq. 1 and taking the curl of the result, we obtain

$$\frac{\partial}{\partial t}\bar{u} + \nabla\times(\bar{u}\times\bar{v}) = 0 . \tag{17}$$

Here, $\bar{u}$ is defined as

$$\bar{u} = \nabla\times\left(v - \frac{\pi\times B}{\rho}\right) . \tag{18}$$

In the absence of a magnetic field, B = 0, Eq. 18 reduces to the conventional Kelvin theorem. A similar theorem appears in Penfield's work.[4] If we replace Penfield's $\bar{p}$ by $m\bar{v}$ and assume a uniform entropy distribution ($\nabla s=0$), we find that

$$\frac{1}{m}u = \nabla\times\left(v - \frac{1}{m}\sum_j \lambda_j\nabla a_j - \frac{\pi\times B}{\rho}\right) , \tag{19}$$

where the λ_j's are Lagrange multipliers, and the a_j's are Lin's variables. Penfield's Eq. (6.193) is identical with our (17), with his $\bar{u}$ given by (19). Our theorem is Penfield's theorem in a sharpened form because the term $\nabla\times\sum_j \lambda_j\nabla a_j$ has dropped out and thus has been demonstrated to satisfy by itself Eq. 17.

H. A. Haus

References

1. P. Penfield, Jr., Frequency and Power Formulas (The Technology Press of Massachusetts Institute of Technology, Cambridge, Mass., and John Wiley and Sons, Inc., New York, 1960).

2. R. M. Fano, L. J. Chu, and R. B. Adler, Electromagnetic Fields, Energy and Forces (John Wiley and Sons, Inc., New York, 1960).

3. P. Penfield, Jr., op. cit., see Eq. 6.242.

4. Ibid., see Eq. 6.245.

E. THE EFFECT OF INTERNAL CURRENTS ON THE PLASMA DENSITY DISTRIBUTION

Radial density profiles were measured in a highly ionized, finite, cylindrical plasma confined by an axial magnetic field. We found that the shape of the density profile differed considerably, the shape depending on whether the end plates of the cylinder were insulating or conducting. The purpose of this report is to explain, at least qualitatively, this difference.

The experimental arrangement, shown in Fig. XI-9, has cylindrical symmetry about its center line. A hollow-cathode discharge, running down the axis of the cylinder, acts

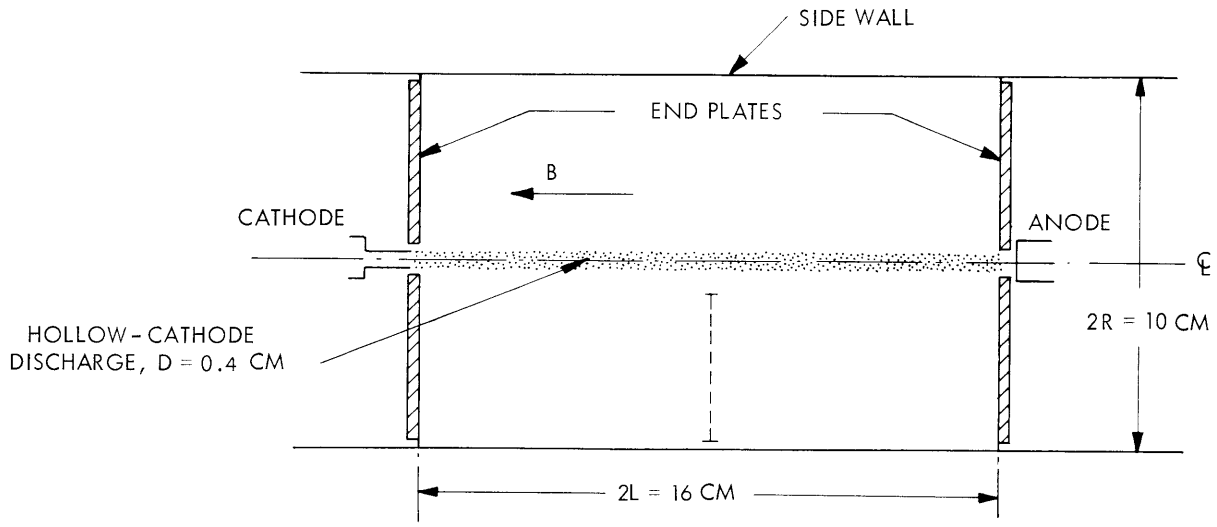

Fig. XI-9. Experimental arrangement.

as a source of plasma for the entire region. The properties of the discharge itself have been described elsewhere[1,2]; and for the purposes of this discussion, the discharge simply supplies an axially uniform plasma density n_o(~ 3×10^{13}/cc) at some small radius r_o(~ 0.2 cm). The side wall of the cylinder is a floating conductor; the end plates may be insulators or conductors and are always electrically isolated from the side wall. The density measurements were made (with Langmuir probes) along a radius at the mid-plane of the cylinder as shown by the dotted line in Fig. XI-9.

The results of such density measurements are shown in Fig. XI-10. The radial coordinate has been normalized to unity at the side wall, and the density normalized to its value at 1 cm from the axis (this is the smallest radius at which probe curves can be made without overheating the probe).

The data shown in Fig. XI-10 are typical of many sets of data taken for various values of axial magnetic fields. The previously indicated difference in the shapes of the profiles is obvious.

From a phenomenological viewpoint, it is obvious that the conducting end plate differs from the insulating plate only in that current can flow within it. Therefore, the effect of the nature of the end plates on the density distribution at the mid-plane should be related to the different current patterns existing throughout the plasma volume and particularly at the mid-plane.

In order to verify this hypothesis, it was necessary to measure the spatial current distributions within the cylindrical volume. This is very difficult to do without creating an excessive disturbance of the plasma. Consequently, we decided to measure the current distribution at the walls of the cylinder and, from these results, attempt to infer

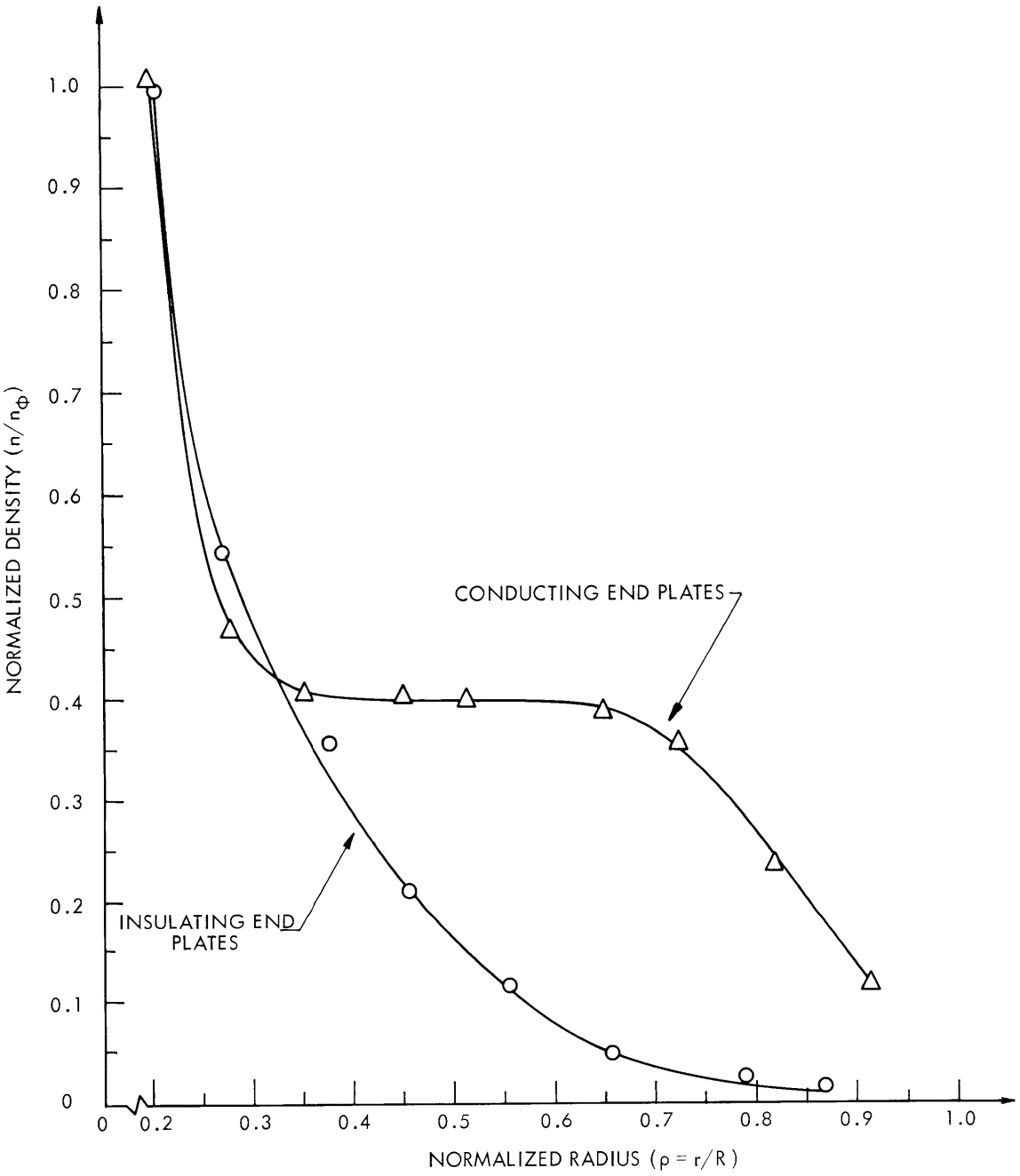

Fig. XI-10. Typical density profiles taken at mid-plane of the cylinder (B = 1025 gauss; $n_o \approx 3 \times 10^{13}$cc).

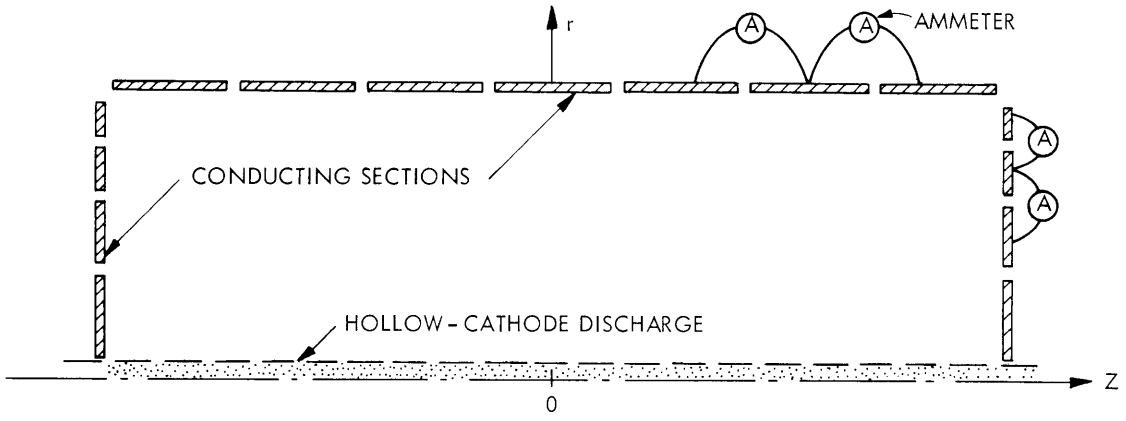

Fig. XI-11. Schematic arrangement used for measuring wall currents. The structure is cylindrically symmetric about the z-axis.

the internal distribution. To do this, the side wall and end plates (when conducting) were divided into conducting sections separated by narrow insulating sections. The sections were connected through dc ammeters. This arrangement, shown in Fig. XI-11, simulates a continuous conductor and also provides a means for measuring the current flow between sections. In this arrangement, as before, the side wall is externally floating and isolated from the end plates.

From the magnitude and direction of the currents measured in the ammeters, and a knowledge of the area of the sections, the average current density entering (or leaving) each plate from the plasma can be calculated. A full set of current measurements was made for various values of magnetic field. Typical results for the direction of the current at each wall section are shown by the arrows at the walls on Figs. XI-12 and XI-13, for insulating and conducting plates respectively. Typical values for the magnitude of the side wall currents are 0.01-1.0 ma/cm^2 and for the end plate currents (when plates are conductors) 1.0-50 ma/cm^2 over a range of magnetic field. In all cases, both side wall and end plate currents decrease with increasing axial magnetic field. The measured asymmetry in wall current patterns (shown in Figs. XI-12 and XI-13) is probably due to the inherent asymmetry of the hollow cathode discharge source which, in this case, carries a current of 40 amps.

Given the directions of the currents on the walls of the cylinder, one can speculate about the internal current patterns. Such speculations, however, must include the following considerations: since the side wall, the end plates, and the source are electrically isolated, the net current entering each must be zero. Also, the flow pattern should be approximately symmetric about the midplane of the cylinder. Based on these considerations, two basic current patterns have been deduced. These are indicated by the dotted lines in Figs. XI-12 and XI-13. The patterns shown are not unique; however, they are reasonably simple and are sufficient to account for the observed difference in

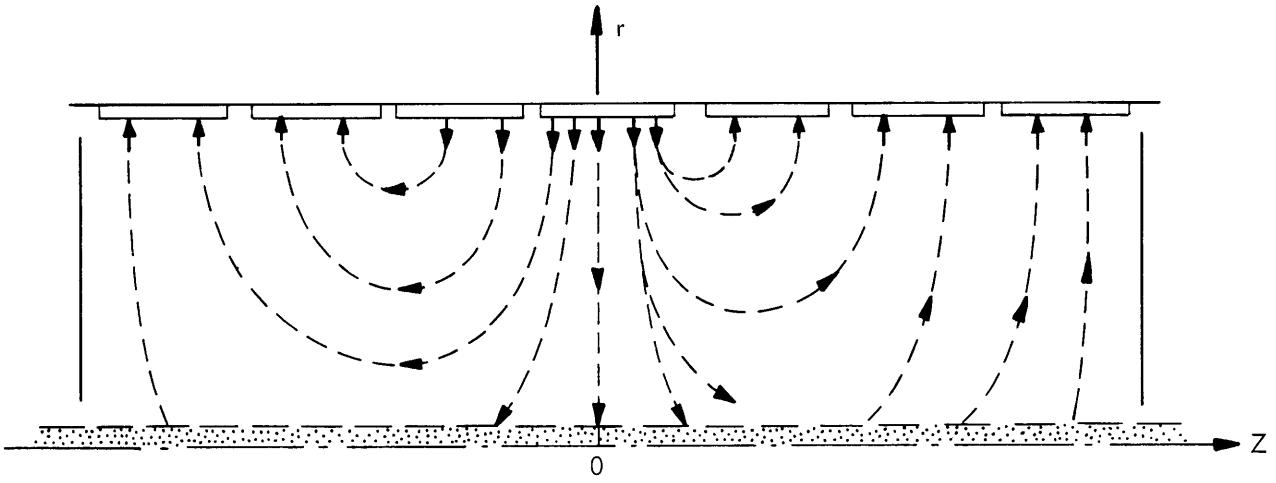

Fig. XI-12. Proposed current pattern for insulating end plates.

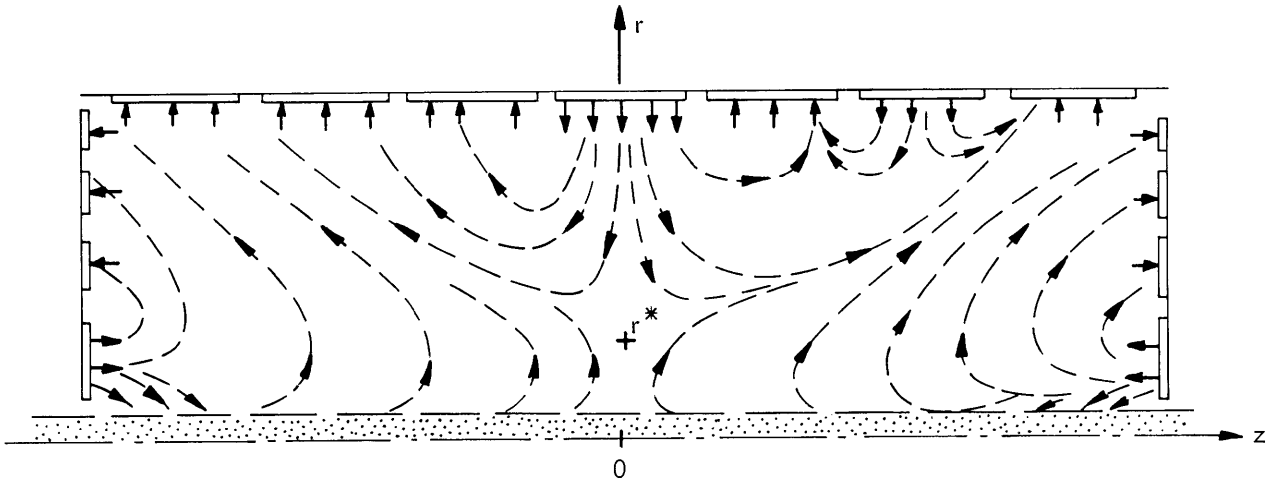

Fig. XI-13. Proposed current pattern for conducting end plates.

in density profiles in the two cases. Upon examination of Figs. XI-12 and XI-13, several characteristics should be noted for later discussion. For insulating end plates (Fig. XI-12), the radial current at the mid-plane (Z = 0) is negative for all values of radius (r). For conducting end plates, there is a value of r at the mid-plane $r = r^*$ which is such that for $r > r^*$, the radial current is negative, and for $r < r^*$ the radial current is positive. This effect is due to current flow in the conducting end plates.

2. Theory

Let us now consider the mathematical analysis of the problem in order to examine the way in which these current patterns affect the plasma density distribution. We

consider a singly charged highly (but not fully) ionized plasma in which the ions and electrons interact, and in which the ions (but not the electrons) interact with the neutral gas. This model is reasonable for an argon plasma produced by the hollow-cathode discharge. This plasma is ionized in excess of 50 per cent; the electron temperature (1-2 ev) is such that the electron-atom collision cross section is very low (near the Ramsauer minimum), and the ion-atom interaction is by charge exchange — a process that has an appreciable cross section. We shall assume, for simplicity, that the plasma is isothermal. Moreover, we shall assume that the axial magnetic field is sufficiently large so that the cyclotron frequency for both electrons and ions is much larger than their respective collision frequencies with other particles. The plasma geometry has azimuthal symmetry.

Under these conditions, it can easily be shown (either by solution of the contiuum momentum equations or by direct expansion and solution of the Boltzmann equation[3]) that the following expressions are valid for the radial, steady-state, ion and electron particle currents (Γ_r^i and Γ_r^e), respectively.

$$\Gamma_r^i = -D\frac{\partial n^2}{\partial r} + \frac{D_g}{e}\left(neE_r - T^i\frac{\partial n}{\partial r}\right) \tag{1}$$

$$\Gamma_r^e = -D\frac{\partial n^2}{\partial r} \tag{2}$$

where

$$D = \frac{\eta}{2B^2}(T^i+T^e) \tag{3}$$

$$D_g = \frac{m_i\nu_{io}}{eB^2} \tag{4}$$

In these expressions, n is the plasma density, B is the axial uniform magnetic field, e is the electronic charge, η is the Spitzer resistivity, T^i and T^e are the ion and electron temperatures, respectively, m_i is the ion mass, ν_{io} is the ion-atom collision frequency, E_r is the radial electric field, and r is the radial spatial coordinate.

We define the radial current density:

$$j_r = e\left(\Gamma_r^i - \Gamma_r^e\right) \tag{5}$$

and by subtracting Eq. 2 from Eq. 1 we find

$$j_r = D_g\left(neE_r - T^i\frac{\partial n}{\partial r}\right). \tag{6}$$

Hence, we can rewrite Eq. 1 as

$$\Gamma_r^i = -D\frac{\partial n^2}{\partial r} + j_r/e. \tag{7}$$

Since we have a steady-state analysis, made outside the source region of Fig. XI-9, the following continuity equations are valid in cylindrical symmetry:

$$\frac{1}{r}\frac{\partial}{\partial r} r\,\Gamma_r^i + \frac{\partial \Gamma_Z^i}{\partial z} = 0 \tag{8}$$

$$\frac{1}{r}\frac{\partial}{\partial r} r\,j_r + \frac{\partial j_Z}{\partial Z} = 0 \tag{9}$$

If we substitute Eq. 7 in Eq. 8 and use Eq. 9, we obtain

$$D\frac{1}{r}\frac{\partial}{\partial r} r\frac{\partial n^2}{\partial r} - \frac{\partial \Gamma_Z^i}{\partial Z} = \frac{1}{r}\frac{\partial}{\partial r} r\frac{j_r}{e} = -\frac{\partial j_Z/e}{\partial Z}. \tag{10}$$

Consider now Eq. 10 evaluated at the mid-plane of the cylinder, that is, at Z = 0. To proceed further, we must evaluate $(\partial \Gamma_Z^i/\partial Z)_{Z=0}$. To do this, we assume that Bohm's criterion is valid for the axial ion current at the end plates, and we make a linear interpolation for the purpose of estimating $(\partial \Gamma_Z^i/\partial Z)_0$. This procedure gives

$$(\partial \Gamma_Z^i/\partial Z)_{Z=0} = \sqrt{\frac{T^e}{m_i}}\ \frac{n}{L}. \tag{11}$$

Substituting Eq. 11 in 10, we obtain, at Z = 0,

$$\frac{1}{r}\frac{d}{dr} r\frac{dn^2}{dr} - Kn = \frac{1}{eD}\frac{1}{r}\frac{d}{dr} r\,J_r = -\frac{1}{eD}\left(\frac{\partial j_Z}{\partial Z}\right)_o, \tag{12}$$

where $K = \frac{1}{DL}\sqrt{T^e/m_i}$.

Let us define

$$J(r) = \frac{1}{eD}\left(\frac{\partial j_z}{\partial z}\right)_o. \tag{13}$$

Then Eq. 12 becomes

$$\frac{1}{r}\frac{d}{dr} r\frac{dn^2}{dr} = Kn - J(r). \tag{14}$$

It is precisely the difference in the function J(r) in the two cases (conducting or insulating end plates) that gives rise to the difference in density profile. Therefore we now proceed to estimate J(r) for the two cases.

For insulating end plates, $j_Z = 0$ at the end plates, and $j_Z = 0$ at the mid-plane, from

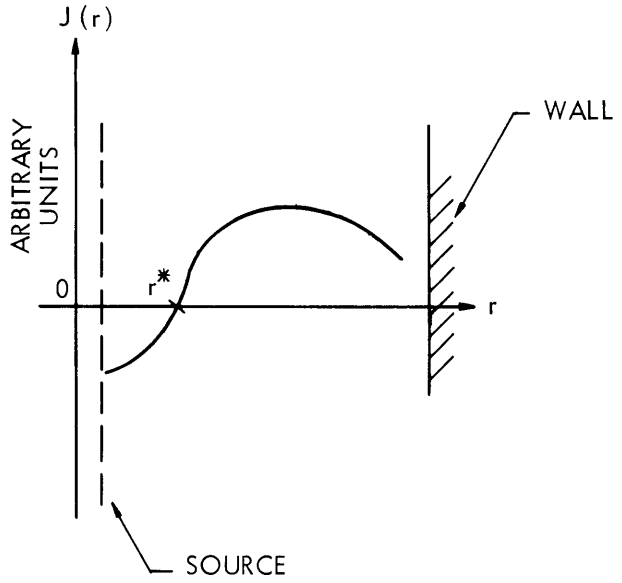

Fig. XI-14. Approximate dependence of $\partial j_Z / \partial Z$ at mid-plane of the cylindrical plasma with conducting end plates, as a function of radial position.

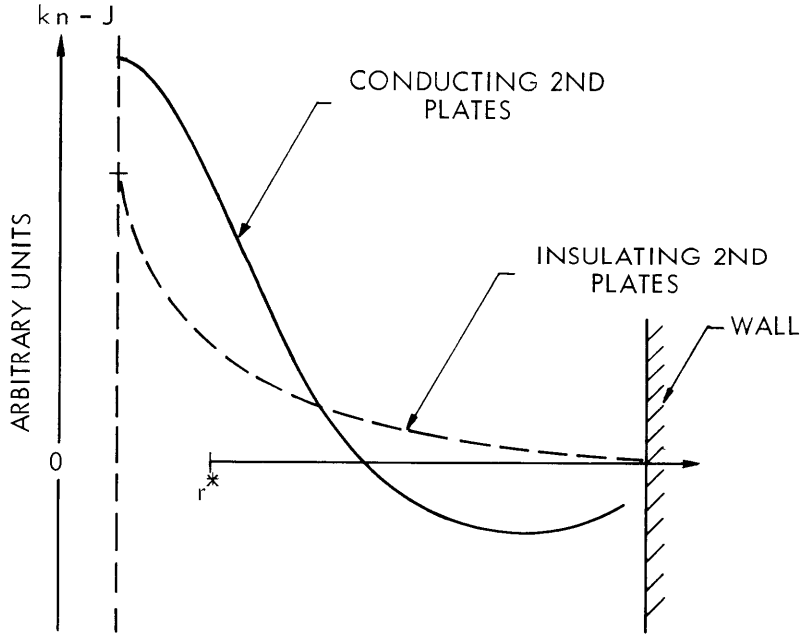

Fig. XI-15. Curvature of n^2 vs r.

symmetry considerations. We shall assume that $j_Z = 0$ for all Z, which leads to the conclusion that, for insulating end plates, J(r) = 0. This result would require that all of the current lines in Fig. XI-12 be radial, which is probably not true. However, it is reasonable to assume that J(r) is very small compared with what it would be for conducting end plates. This less restrictive assumption only requires that the current lines in Fig. XI-12 be almost completely radial in the neighborhood of the mid-plane, and this is sufficient for the argument that follows.

When we consider conducting end plates, we can no longer say that j_Z vanishes on the end plate, although we can still use the symmetry argument at the mid-plane. We can obtain information, however, from examination of Fig. XI-13. Note that for $r < r^*$, $(\partial j_Z/\partial Z)_o < 0$; and for $r > r^*$, $(\partial j_Z/\partial Z) > 0$. It is impossible to obtain numerical values for derivatives of the internal currents, but it is not unreasonable to assume that a plot of J(r) vs r, for conducting end plates, might appear as shown in Fig. XI-14.

If we note that n(r) is always a monotonically decreasing function of r, we can estimate the right hand side of Eq. 14, which is proportional to the curvature of n^2, for the two cases. Such estimates are shown in Fig. XI-15. We see, from Fig. XI-15, that for insulating end plates the curvature of n^2 is always positive and is a decreasing function of r, whereas, for conducting end plates, the curvature starts positive, goes through zero and then goes negative. This behavior corresponds exactly to that exhibited by the data as depicted in Fig. XI-10.

S. D. Rothleder

References

1. D. J. Rose, L. M. Lidsky, S. D. Rothleder, and S. Yoshikawa, Experimental results on the hollow-cathode discharge, Quarterly Progress Report No. 58, Research Laboratory of Electronics, M. I. T., July 15, 1960 pp. 41-44.

2. L. M. Lidsky, S. D. Rothleder, D. J. Rose, S. Yoshikawa, C. Michelson, and R. J. Mackin, Jr., Highly ionized hollow-cathode discharge, J. Appl. Phys. (in press).

3. J. P. Wright, Phys. Fluids 4, 1341 (1961).

F. PRODUCTION OF ION BEAMS

An experiment designed to produce an ion beam of approximately 50 ma of molecular hydrogen ions at 50 kv suitable for injection into a "corkscrew" device is near completion.

In order to fully utilize the trapping properties of a helical magnetic field, the injected beam must have both low divergence and low energy spread. The latter criterion is met by a von Ardenne[1] ion source which, in addition to its high efficiency, will also give the required current. However, the normal method of extraction from this source gives a highly divergent beam of approximately 8° half-angle, but we hope to overcome this by means of the extraction system shown in Fig. XI-16. The combination of the cusped

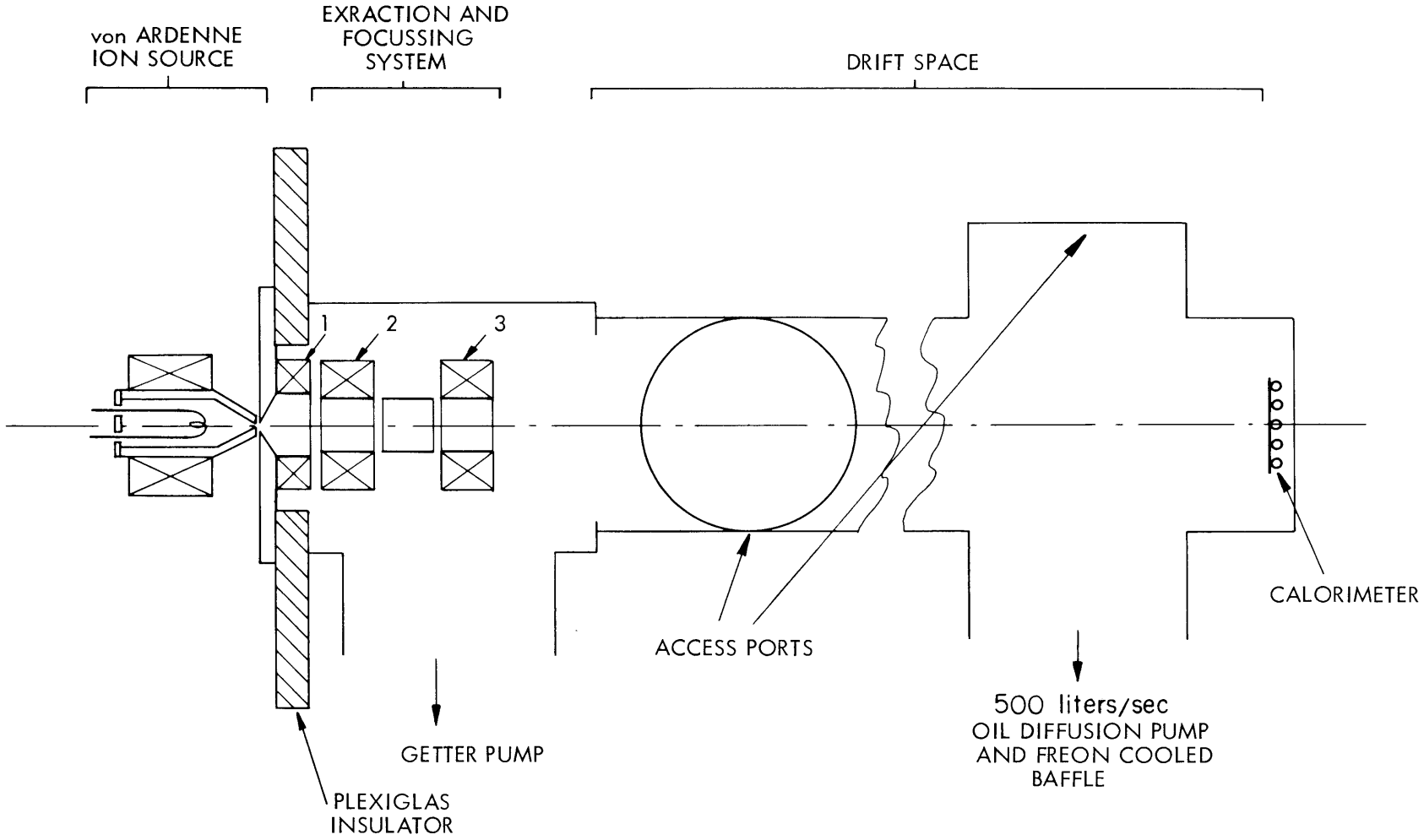

Fig. XI-16. Schematic view of apparatus for the production of low-divergence ion beams.

magnetic fields from coils 1 and 2 with the electrostatic accelerating field gives a concave plasma boundary from which the ions are extracted; the result is an initially convergent beam.

Some measure of success was obtained with the use of this general scheme, in August 1961, by the author at A. W. R. E. Aldermaston, where 30-kv beams of approximately 6 ma with divergence of 3° half-angle were produced. We hope that better performance will be obtained with this system which includes a short-focus electrostatic lens, the center element of which is in the magnetic-mirror field formed by coils 2 and 3. This may result in (a) reduction of electron loss from the beam to the central element, and (b) the trapping of some electrons in the center of the lens which will help to neutralize the ion space charge in this region.

Both of these effects should reduce the space-charge blow-up of the ion beam.

In order to maintain a high vacuum in the vicinity of the extraction and focusing electrodes, the center element of the lens is constructed of stainless-steel mesh and the region pumped by a getter pump designed for this purpose.

If space-charge blow-up of the beam is still excessive because the lens draws too many electrons from the beam, a magnetic lens will be used.

The construction of the experiment is almost complete, and the ion source has operated satisfactorily. We hope to try the extraction and focusing system soon.

E. Thompson

References

1. G. G. Kelley, N. H. Lazar, O. B. Morgan, Nuclear Instruments and Methods 10, 263-271 (1961).

2. W. A. S. Lamb and E. J. Lofgren, Rev. Sci. Instr. 27, 907 (1956).

G. LARGE-VOLUME SUPERCONDUCTING SOLENOID

The large-volume superconducting solenoid described in previous reports[1,2] is now in the final stage of construction. Some parts such as the main containing vessel, are finished and vacuum leakproof tested. Most of the other parts are ready to be assembled. Figure XI-17 shows the vessel in the helium leak test station of the Research Laboratory of Electronics. Approximately 60 per cent of the 100 pounds of niobium-zirconium that has been ordered is already on hand; the remainder is due to arrive within the next few weeks.

During this period we have investigated the behavior of numerous small superconducting solenoids.

Although the situation is far from clear, various interesting bits of information have been obtained.

Fig. XI-17. Large-volume superconducting solenoid.

(i) Insulated-Wire Versus Bare-wire Solenoids

Several experiments were undertaken to see which one of these two concepts is the more promising. Indeed, Berlincourt and his co-workers have recently reported superconducting solenoids wound with bare wire. We have found:

(a) Bare-wound solenoid implies much longer rise time than insulated wire solenoids — 20 minutes versus 1 minute. Also, the quenching current seems to be less reliable for the bare-wire than for the insulated-wire solenoid.

(b) Some appreciable amount of the magnetic field is always lost by occasional superconducting shorts, and therefore the magnetic constant ratio (MCR) is highly unpredictable and the direct measurement of the magnetic field through the value of the current is not possible.

(c) The release of the magnetic energy is much quicker for the bare-wire type than

for the insulated-wire type, which makes the first concept less safe than the second one.

Therefore we definitely shall use an insulated-wire solenoid for our large apparatus. Various dielectric insulator materials have been tested: nylon fabrics fused, polyurethane, formvar and polyester enamels. All of the enamels behave quite well, but on the basis of hardness and strength we shall use polyester enamel.

(ii) Voltage Surge Caused by Quenching

This factor can cause breakdown of the insulation and burning or annealing of the superconducting wire. An internal shunt or rheostat built into the power supply appears to be a simple and practical solution. In any case, the peak voltage is no more than $R_{ES} I_q$, where R_{ES} is the shunt resistance, and I_q the quenching current (between 15 and 25 Amps for 10-mil wire). Moreover, the external shunt permits an easy control of the rise time of the magnetic field, the time constant being L/R_{ES}. This is very helpful for increasing the quenching up to its highest possible value.

With this arrangement, up to 30 successive quenchings have been made on a given solenoid without any visible damage to the solenoid.

(iii) Energy Dissipation during Quenching

Solenoids up to 1 kJ of magnetic energy stored have been tested. It appears that the release of this energy is much slower than we had thought, probably because of the high thermal impedance of the winding. For solenoids immersed in helium, it takes from 1 to 3 minutes to cool down the solenoid after quenching it and to be in a position to start it again.

The addition of a copper winding has been found to be quite effective for removing part of the magnetic energy from the liquid-helium space. For a bifilar winding, this effectiveness is close to 100 per cent. It seems that the addition of a few layers of copper-wire winding inside and outside the superconducting winding is a compromise between simplicity of construction and efficiency. This protecting coil is of great interest for the safe and economical operation of a superconducting solenoid, since it limits the effect of quenching voltage and also the amount and the rate of the magnetic energy dissipated in the liquid-helium bath.

(iv) Penetration of the Magnetic Field inside a Superconducting Solenoid

Experiments seem to indicate that the field penetrates the inside space not by a continuous and regular process but by jumps as recorded by an oscilloscope or a microvoltmeter. This phenomenon may be related to the early quenching of some solenoids, because of the disastrous effect of fast current change on the superconducting state of the material.

(v) Decrease of the Current with the Size and the Strength of the Solenoid

Although this assertion presents as many exceptions as rules, it seems that there is a definite trend toward low current density when the size and the strength of the solenoid increase. Let us take an example: a 0.050-in. I. D., 3.0-in. long, 30-kGauss solenoid is operable at a reliable current of 16 Amps; a 0.5-in. I. D., 3.0-in. long, 60-kGauss or 2.0-in. I. D., 8.0-in. long, 30-kGauss solenoid is limited to ~10 Amps.

The cause or causes, thus far, are quite confusing and may include items such as the quality of the material, the effectiveness of the dielectric insulation, the proximity effect, the length of the superconducting wire, and the sensitivity of connections to the magnetic field.

Since the design of our solenoid calls for 24 different spools, the length of wire in each will be limited to approximately 18,000 feet. The wire will be the insulated wire with a polyester enamel, which seems to have less porosity than the nylon fused insulation wire used in most of our experiments with small solenoids. The connection will be positioned in the low-field region of the solenoid, that is, outside the magnet close to the equatorial plane. A magnetic shielding will be provided to reduce the magnitude of the stray field still further.

We hope that these arrangements will give maximum effectiveness and safety for the operation of our large solenoid.

L. J. Donadieu

References

1. D. J. Rose and L. J. Donadieu, Quarterly Progress Report No. 62, Research Laboratory of Electronics, M.I.T., July 15, 1961, pp. 68-72.

2. L. J. Donadieu and D. J. Rose, Proceedings of the International Conference on High Magnetic Fields (The M.I.T. Press, Cambridge, Mass., and John Wiley and Sons, New York, 1961), pp. 358-369.

H. ENERGY EXTRACTION BLANKET FOR A FUSION REACTOR

The configuration of the blanket system has been considerably refined since our last discussion of this problem.[1] The system to be used in detailed calculations is illustrated in Fig. XI-18. The innermost thermal barrier will separate the fused-salt cooled region from a low-temperature water-cooled shielding region. All neutrons and heat leaking beyond this barrier will be discarded. The thickness of the high-temperature fused-salt region will be determined by the neutron leakage, since neutron economy is more critical than heat economy.

The coil shielding region will protect the superconducting magnetic coils from excessive nuclear heating. The heating of the magnet and its 10 cm of stainless-steel

structural support will have to be less than 10^{-5} of the total nuclear heat. Otherwise, the energy required to cool the magnet will seriously affect the over-all energy balance. Maintaining the coil shielding region at low temperature permits the use of efficient neutron and gamma attenuators such as borated water and lead.

1. Heating and Heat Transfer

An unavoidable economic disadvantage of foreseeable thermonuclear reactors is a very large ratio of peak-to-average power (here we mean spatial distribution, not time distribution). This problem, inherent in systems composed of a reaction chamber surrounded by an energy-conversion region, results in high capital costs for the available output power. The questions of heating and heat transfer are therefore of major importance in the economy of thermonuclear power.

Codes in IBM 7090 Fortran language are being developed to calculate heating rates in the blanket structure. Heating rates are of particular importance in two regions, the first wall and the magnet coils. Cooling of the first wall will place an upper limit on the

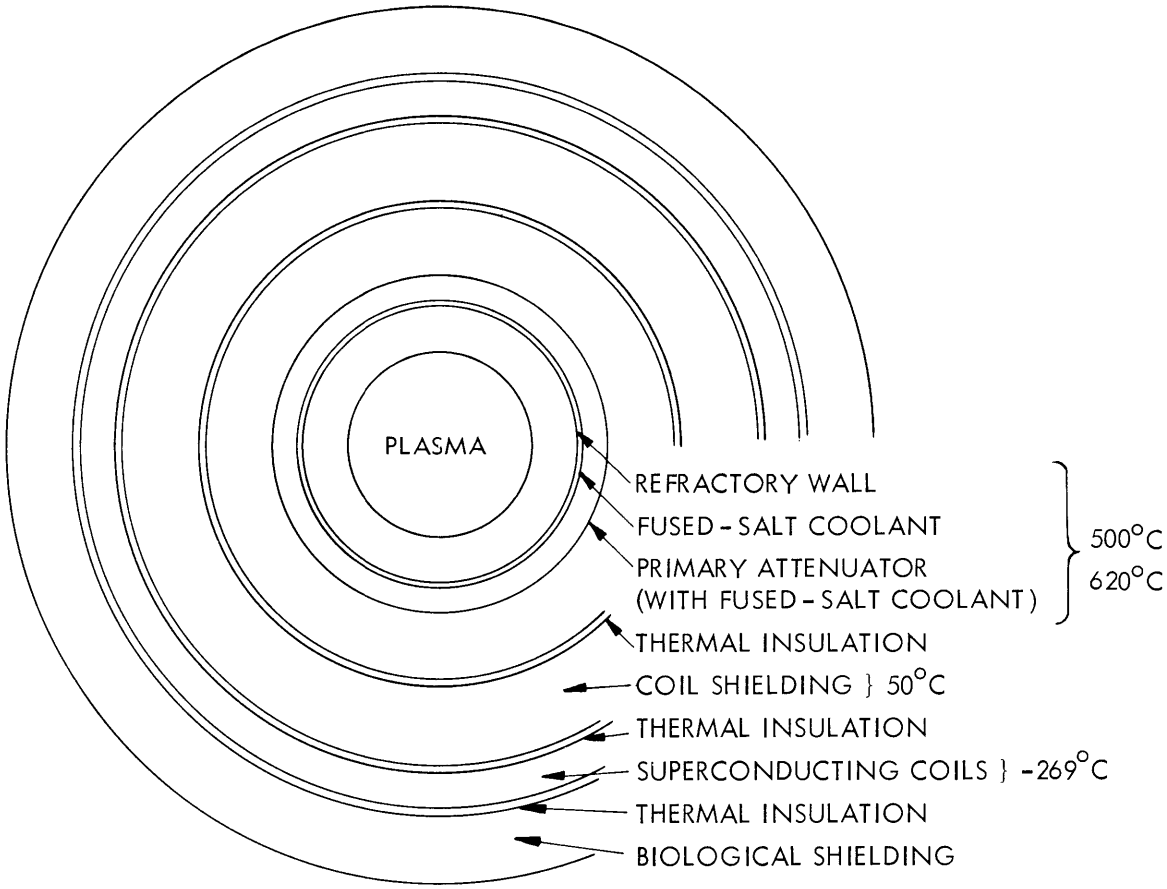

Fig. XI-18. Functional arrangement of the blanket.

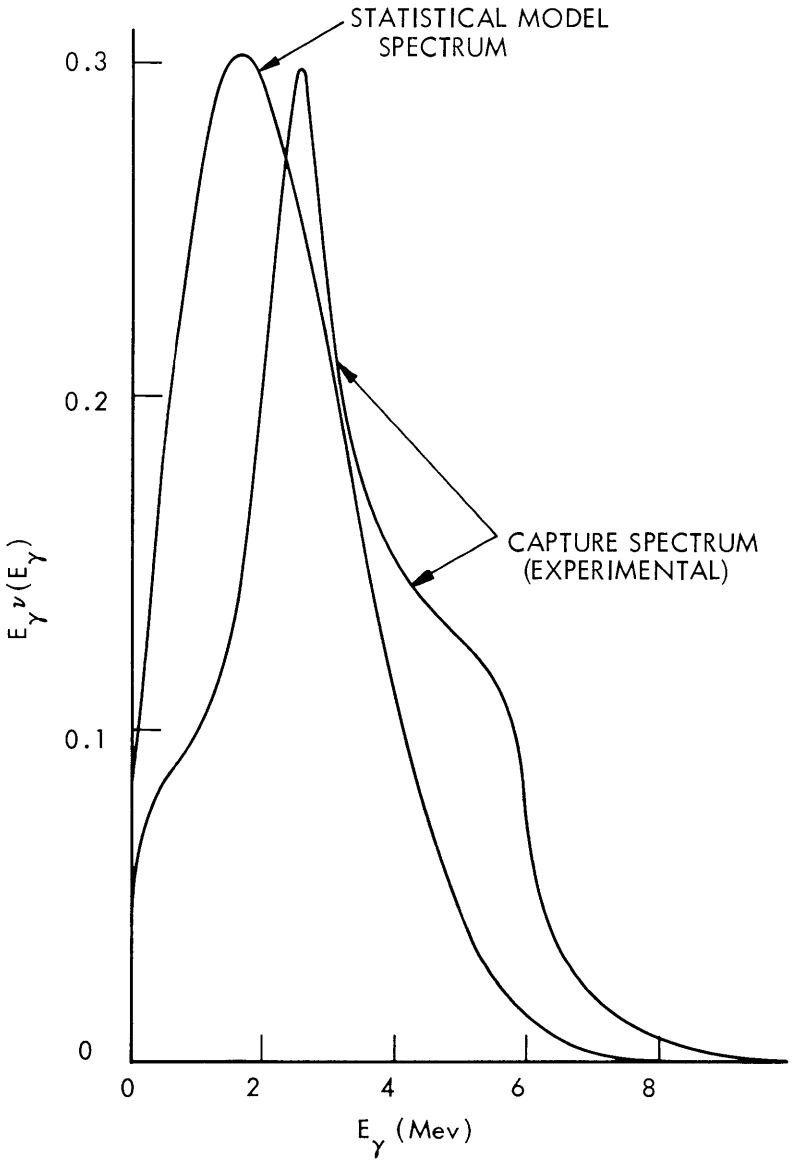

Note: Capture spectra are obtained from Groshev et al.[4] by averaging over peaks. The ordinate scale of photon energy emitted per unit energy is normalized to make the area under the curves (total energy) equal 1.

Fig. XI-19. Calculated and measured spectra for Cd^{114}.

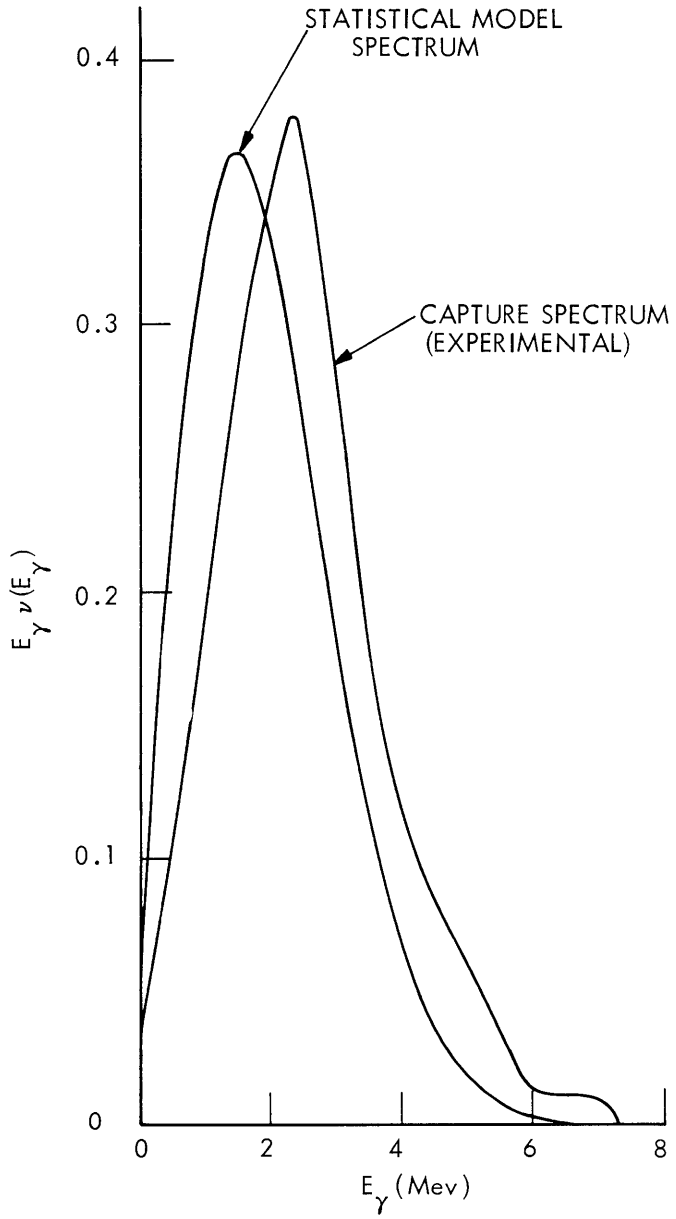

Note: Capture spectra are obtained from Groshev et al.[4] by averaging over peaks. The ordinate scale of photon energy emitted per unit energy is normalized to make the area under the curves (total energy) equal 1.

Fig. XI-20. Calculated and measured spectra for Sm^{150}.

energy density in the thermonuclear plasma, limiting the power output from a given structure. Heating in the magnet will determine the necessary thickness of coil shielding which represents an important contribution to the capital cost.

Since a large fraction of the nuclear heat is liberated by secondary gammas from nonelastic neutron interactions, the heating-rate codes must allow estimation of the spectrum of these photons in addition to providing accurate approximations to gamma transport. The spectrum of photons from heavy nuclides is being calculated from the statistical model, with the assumption of a continuum of levels of the emitting nucleus. As shown in Figs. XI-19, XI-20 and XI-21, this approximation underestimates the energy of the gammas. The model will be useful, however, in estimating the relative effect of initial nuclear excitations that are either higher or lower than the binding energy of the neutron (Fig. XI-22). It is for these cases that no experimental data exist.

Gamma transport is being approximated by two methods with the intention of comparing the results. The first method is a build-up factor approach, based on the moments method calculations of Goldstein and Wilkins.[2] Eight energy groups are being used with infinite slab geometry approximating the actual cylindrical shells. Energy absorption build-up factors for monoenergetic point isotropic photon sources are being approximated by a sum of exponentials to permit their application to slab geometry.

Build-up calculations of this type do not break down at large distances from gamma sources and are exact for infinite homogeous media. In heterogeneous media, for which suitably averaged build-up factors must be used, heating in high Z materials is underestimated, while heating in low Z materials is overestimated. In addition, photon energy is not necessarily conserved.

The second gamma transport approximation that is being employed is a one-group method in which an averaged energy absorption coefficient is used as an attenuation coefficient. The energy absorption coefficient for each absorber nuclide is averaged over the energy spectrum of the emitted photons. This method incorporates the assumptions that the photon spectrum is constant regardless of distance from the source and that all scatterings are straight ahead. It is quite accurate near the gamma source, and automatically conserves total energy. Beyond a few mean-free paths from the source, however, it can be expected to err seriously.

The build-up factor method is obviously the better one for calculation of heating in the magnet. It may be inferior, however, for the estimation of first-wall heating.

2. Neutronics Calculations

Several revisions have been made in the digital computer codes developed for neutronics calculations, and several new configurations have been explored. A low-energy code, run in conjunction with the higher energy code mentioned in a previous report,[1]

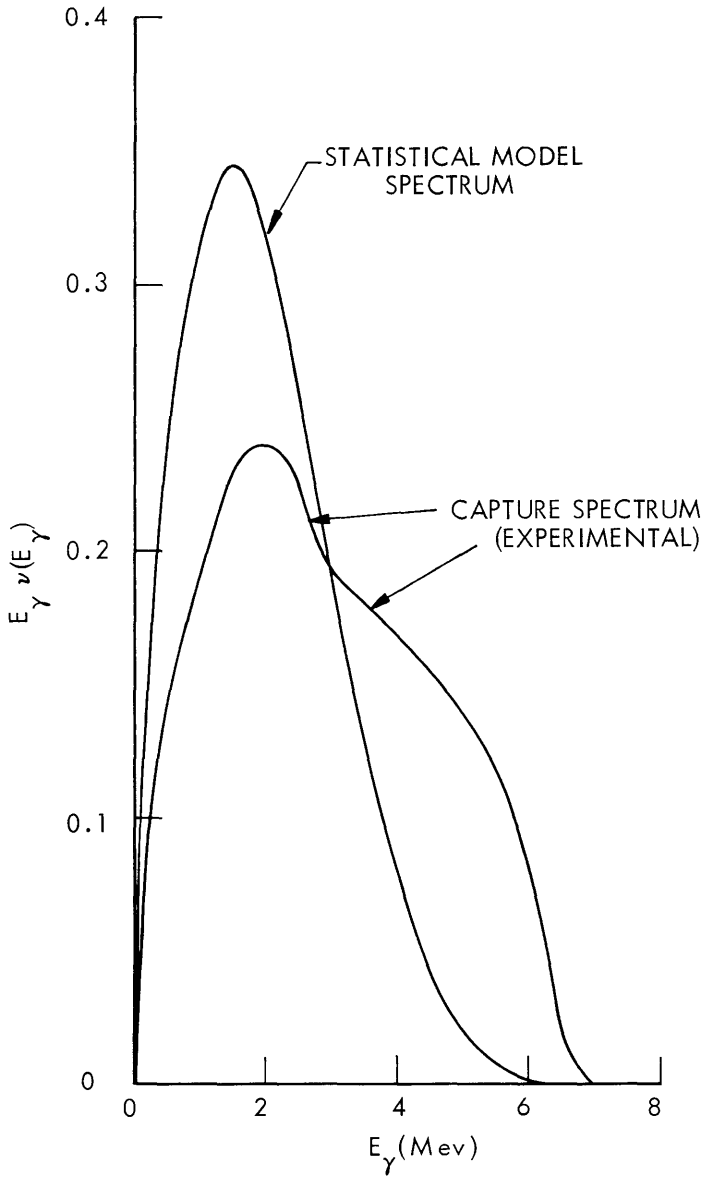

Note: Capture spectra are obtained from Groshev et al.[4] by averaging over peaks. The ordinate scale of photon energy emitted per unit energy is normalized to make the area under the curves (total energy) equal 1.

Fig. XI-21. Calculated and measured spectra for Rh^{104}.

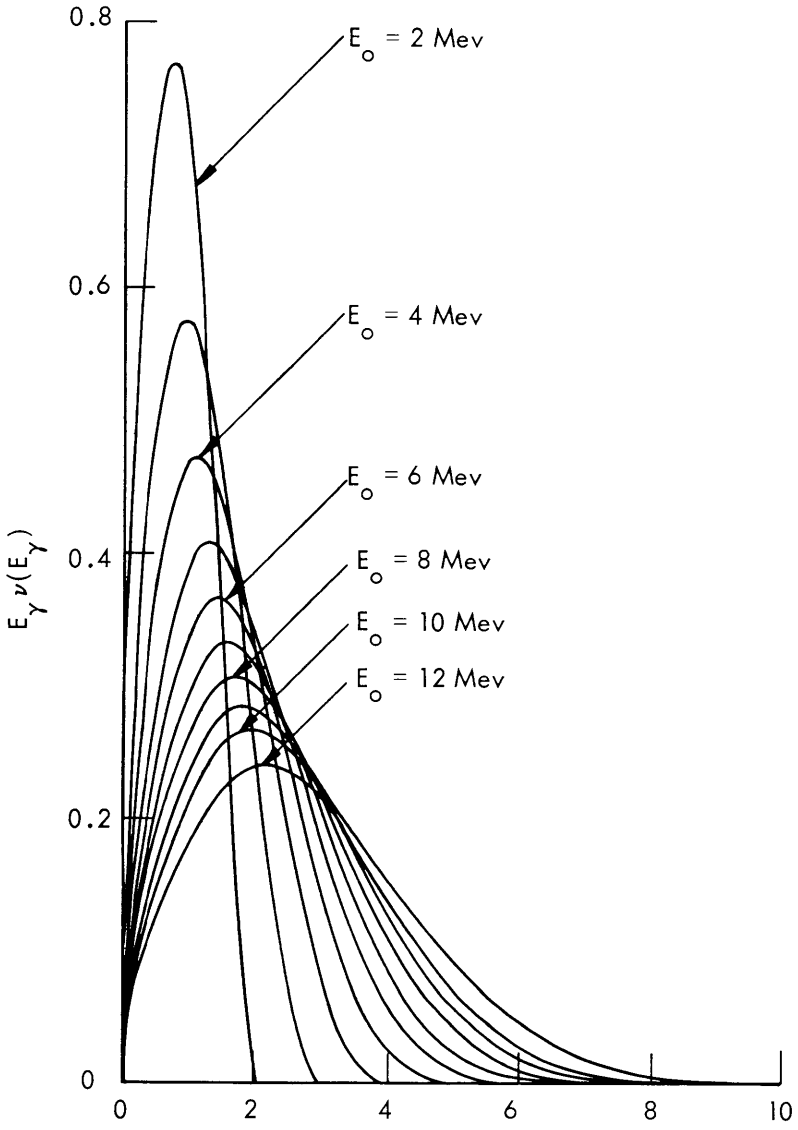

Note: Capture spectra are obtained from Groshev et al.[4] by averaging the peaks. The ordinate scale of photon energy emitted per unit energy is normalized to make the area under the curves (total energy) equal 1.

Fig. XI-22. Effect of initial excitation on gamma spectrum from molybdenum-continuous statistical model.

allows calculation of neutron flux distributions in 50 lethargy groups extending from 14.2 MeV to thermal energies with explicit treatment of resonance-induced volume and surface absorption of neutrons. Also, the calculations may now be carried out by using either the approximation to integral transport theory previously noted,[1] or the "S_n" differential transport approximation. Test cases that have been run to compare the results of integral and differential transport calculations yield results that differ by 1 per cent, or less, in tritium breeding ratio. The treatment, at present, is still limited to a 3-region configuration, although a 5-region code is now being developed.

The extended codes have been applied to a physically practical system consisting of a molybdenum first wall, 1-cm thick, a first-wall coolant channel, 5-cm thick, containing $2LiF \cdot BeF_2$, and a primary attenuator region, 30-cm thick, composed of 75 per cent (by volume) $2LiF \cdot BeF_2$ and 25 per cent graphite. The results of these calculations indicate that a tritium breeding ratio of 1.15 (tritons regenerated per triton burned) is attainable, provided that the neutrons appearing in this calculation as leakage through the boundary of the primary attenuator region are not ultimatley lost.

Calculations reported previously[3] indicated that an additional 30 cm of 75 per cent fused salt and 25 per cent graphite will yield (n,t) reactions for essentially all of the neutrons that appear as leakage in the present calculations.

Preliminary estimates of tritium loss rates in a power-generating fusion reactor complex have been made. The largest single loss of tritium is associated with the need to repeatedly recirculate and re-inject fuel particles because of the low burn-up expected in the plasma. Assuming a burn-up of 0.1 and 0.99 recovery in the tritium pumps, we expect a net loss of approximately 10 per cent in tritium. An additional tritium loss of approximately 3 per cent is expected on account of radioactive decay of the tritium inventory in the blanket and incomplete recovery of tritium from the fused-salt mix. The total loss of tritium per pass is not expected to exceed 15 per cent. For these reasons, the blanket configuration noted above (with an extended primary attenuator) should just be able to offset anticipated tritium losses in the rest of the system and to make the proposed fusion reactor independent of external sources of tritium after start-up. The tritium breeding ratio can be further increased by using a somewhat thicker molybdenum first wall, or by introducing beryllium in the primary attenuator. In particular, calculations have shown that an additional 0.09 in tritium breeding can be gained by including the equivalent of 5 cm of beryllium in the primary attenuator region behind a 1-cm molybdenum first wall.

Mention has been made[1] of the possibility of obtaining some tritium without loss of neutrons from reactions of the form $Li^7 + n \rightarrow n + H^3 + He^4$. At the time when this possibility was first considered, no published data were available concerning the $Li^7(n,t)$ cross reaction, and the 2 per cent contribution to the tritium breeding ratio previously cited was based on estimated cross sections. Recently, measured $Li^7(n,t)$ cross

sections over the energy range of interest have been declassified and published. These values, which are rather larger than estimated, have been incorporated into the calculations discussed above. The resultant Li^7 contribution to the tritium breeding ratio is approximately 0.11 in the system discussed above. The calculations also show that the ratio of consumption of Li^6 to Li^7 will be approximately 8:1, so that the fused-salt make-up will necessarily contain lithium almost fully enriched in Li^6.

Auxiliary calculations have been made to estimate the maximum tritium breeding ratio obtainable in blanket configurations that exclude fissile nuclides. The first case considered was that of an 8-cm lead first wall followed by a 3-cm fused-salt coolant channel and a primary attenuator of 75 per cent fused salt plus 25 per cent graphite. This configuration tends to maximize (n, 2n) multiplication of neutrons and yielded a calculated tritium breeding ratio of 1.63.

In the second case, a beryllium first wall, 3-cm thick, was substituted for the lead with the remainder of the system unchanged in an attempt to increase the Li^7 (n, t) contribution to the tritium breeding ratio while taking advantage of the (n, 2n) multiplication in beryllium. The calculated breeding ratio was found to be 1.42 of which only approximately 0.11 is attributable to Li^7 reactions. This configuration is actually somewhat less than optimum; the small gain attributable to Li^7 (n, t) does not compensate for the greater loss in Be(n, 2n) multiplication necessitated by the use of a relatively thin first wall.

Finally, a calculation was made on a hypothetical system involving no first wall, but otherwise identical to those discussed above. In this case the Li^7 (n, t) reaction contributed 0.13 to the tritium breeding ratio. In view of the competing cross sections in Li^7 and in the other constituents of the fused salt, it appears evident that the Li^7 (n, t) reaction will account for no more than 0.12 of the tritium breeding ratio in any practical blanket.

It should be noted that the three cases discussed here were all exploratory in nature and that neither lead nor beryllium appears to be suitable for a first-wall material because of physical limitations.

W. G. Homeyer, A. J. Impink, Jr., D. J. Rose

References

1. W. G. Homeyer and A. J. Inpink, Jr., Quarterly Progress Report No. 64, Research Laboratory Of Electronics, M.I.T., January 15, 1962, pp. 128-132.

2. H. Goldstein and J. E. Wilkins, USAEC Report NYO-3075, 1954.

3. W. G. Homeyer, A. J. Impink, D. J. Rose, and I. Kaplan, Quarterly Progress Report No. 62, Research Laboratory of Electronics, M.I.T., June 15, 1962, pp. 64-68.

4. L. V. Groshev, Atlas of Gamma Ray Spectra from Radiative Capture of Thermal Neutrons (Pergamon Press, New York, 1959).

I. DESIGN AND CONSTRUCTION OF PULSED PLASMA ACCELERATOR

The interaction of a traveling magnetic wave and a stationary plasma is now under study. The magnetic wave (of up to 5000 gauss) travels at a velocity of 1.7×10^7 cm/sec through a region filled with a dense, highly ionized, low-temperature plasma. The plasma generation and confinement schemes and the relevant plasma parameters have been discussed in previous reports.[1,2] The magnetic wave is generated by the passage of a current pulse along a helical "delay line" surrounding the plasma. The design and construction of a line capable of generating a 5-kGauss magnetic pulse will be discussed in this report.

1. Design Considerations

Consider the line shown in Fig. XI-23. The magnetic field generating helix of radius r is in intimate contact with a thin cylindrical dielectric shell of thickness d which, in turn, is surrounded by a grounded conducting cylinder. If we demand that the dielectric material be fully utilized (i.e., stressed to break down), then d may be expressed in terms of the applied voltage, E, and the dielectric strength S. The capacity/unit length, C, is given by

$$C = \frac{2\pi r \epsilon_o KS}{E}, \tag{1}$$

where K is the dielectric constant of the material.

It is apparent that if the separate turns of this helix are to act in concert to produce

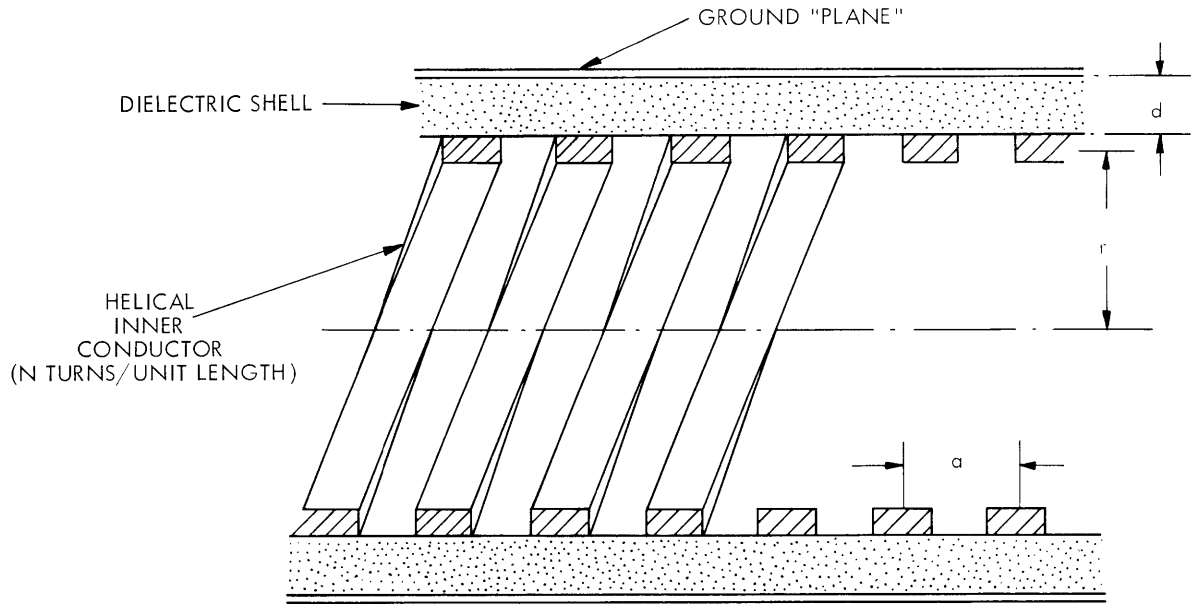

Fig. XI-23. Dielectric shell model.

Table XI-1. Figures of merit for several dielectric materials.

Material	K	S (v/mil)	KS (v/mil)
Nylon	3.5	470	1.64
Polystyrene	2.5	600	1.50
Vinyl chloride	4.0	900	3.60
Steatite	6.5	300	1.95
Barium titanate	2.5×10^3	125	>300

the magnetic field of the traveling wave, they must also interact with each other. The inductance of the helix per unit length will depend on the parameters of the helix itself and those of the wave that is being propagated. For a closely coupled coil, we expect the effect of magnetic coupling to be important over lengths that are about that of the rise length of wave, for it is precisely this region over which rapidly changing currents make (mutual) inductive effects important. Considering that the minimum rise length of a well-designed system will be of the order of the radius of the coil and assuming very tight coupling, we take the inductance/unit length, L, to be

$$L = N\,\ell(r/a) = \ell\, r/a^2, \tag{2}$$

where N is the number of turns per unit of length, and ℓ is the self-inductance of a single loop.

If we consider a pulse long in spatial extent compared with the radius of the helix and use Eqs. 1 and 2 to express the result in terms of quantities of interest, we find

$$B \approx \mu_o\sqrt{2\pi\epsilon_o E/\ell}\cdot (KS)^{1/2}, \tag{3}$$

or alternatively

$$B \approx (2\pi r\epsilon_o\mu_o V/a)\cdot (KS), \tag{4}$$

where V is the velocity of pulse propagation. The product of dielectric constant and dielectric strength thus defines a "figure of merit" for our application. Inspection of Table XI-1 (listing some representative values of this product) virtually compels the use of some (Ba-Sr)TiO_3 ceramic dielectric. We decided to use a compound (T-176A) manufactured by the American Lava Company with a KS product of 475 kv/mil. Once the dielectric properties are fixed, it is a simple matter to estimate the magnitude of the traveling field that could be generated by the idealized system under consideration. For example, if we choose $V = 10^7$ cm/sec., E = 25 kv, and let the size of the remainder of the experimental system hold $r \approx 4.5$ cm, we find

$$B_{max} \approx 6000 \text{ gauss.} \tag{5}$$

There seems to be no question that a modified high-voltage delay line is capable of producing fields of sufficient magnitude to ensure strong interaction with any reasonable plasma column.

2. First-Order Analysis

The interaction of a traveling magnetic wave with a stationary plasma is a strong function of V, the wave velocity because the particle energy in the moving frame of reference defined by the pulse is dependent upon V^2. The dependence of the interaction on the magnitude of B may be either first-power (adiabatic reflection) of second-power (magnetic-kinetic pressure balance). In either case, it is evident that we must be able to predict the behavior of the traveling-wave line with much greater confidence than could be inferred from the simple continuously distributed parameter model discussed here. Two models, the first based upon the dispersion equation for wave propagation, the second on a numerical solution of the coupled second-order equations of the system, have been developed.

a. Dispersion Equation

As is well known, the dispersion relation for waves propagating in a simple lumped LC delay line with no inductive coupling between sections is given by

$$\omega^2 CL = 2(1-\cos k), \tag{6}$$

where L is the inductance of a single section, C is the capacitance of a section, and the wave vector, k, is given by $2\pi a/\lambda$ for spacing a and wavelength λ. For an inductively coupled system, we may write[3]

$$\omega^2 C\left[L + 2\sum_{n=1}^{\infty} L_n \cos(nk) \right] = 2(1-\cos k), \tag{7}$$

where L_n is the mutual inductance between n^{th} neighbors. It is apparent that we may recover the form of the simpler case simply by redefining the inductance or, more explicitly, by setting

$$L' = \gamma_k L = \left[1 + \frac{2}{L}\sum_{n=1}^{\infty} L_n \cos(nk) \right] L . \tag{8}$$

If we restrict ourselves to wavelengths that are long compared with the spacing of the elements, γ_k is independent of wavelength and the simple expressions for velocity, V_o, and impedance, Z_o, of a continuous line may be used.

$$V = \gamma_o^{-1/2} V_o \tag{9a}$$

$$Z = \gamma_o^{1/2} Z_o \tag{9b}$$

Inserting the expression for the inductance of circular coaxial loops yields

$$\gamma_o = 1 + \frac{\beta(a)}{\left[\ln\left(\frac{8r}{h}\right) - 2\right]}, \tag{10}$$

where $\beta(a) = \sum_{n=1}^{\infty} 2k^3 C$, C is the complete elliptic integral discussed by Jahnke and Emde,[4] $k^2 = 1/\ell + a^2 n^2$, and $a = a/2r$. In this expression, h is the "equivalent radius" of the conductor. A plot of $\beta(a)$ as a function of a is given in Fig. XI-24.

The validity of our low-frequency approximation is illustrated by the comparison

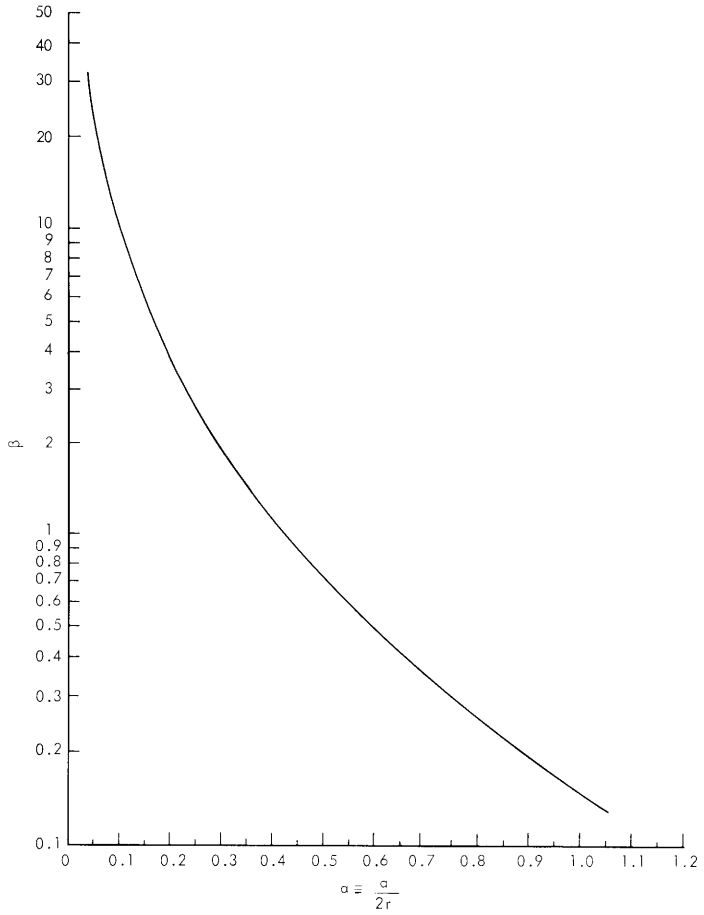

Fig. XI-24. Plot of $\beta(a)$ against a.

Table XI-2. Comparison of experiment and theory for two test lines.

L	L (mμh)	C (mμf)	r (cm)	a (cm)	V_o (cm/sec)	V (cm/sec)	V_{exp} (cm/sec)
Line I	127	10.0	3.81	1.36	4.18×10^7	2.46×10^7	2.3×10^7
Line II	1168	4.70	3.81	0.60	2.13×10^7	0.97×10^7	1.0×10^7

of predicted and experimental values of velocity and impedance for two low-voltage test lines. This comparison for velocity is made in Table XI-2. Besides the rather good agreement of experiment and theory, it is interesting to note that the application of simple lumped-parameter theory leads to an overestimate of $B^2 V^{-2}$ (a measure of interaction strength) by more than an order of magnitude.

b. Inductance Matrix

Consider a line formed of N not necessarily identical LC sections. The line is to be driven by a pulse from a capacitor bank of capacitance C_o and inductance L_o. The line is terminated with a simple resistor, R (see Fig. XI-25). We may write two sets of equations on the x_i's, the first time derivatives of the currents. M_{ij} is taken to be the mutual inductance of the i^{th} and j^{th} loops, so that, for instance, M_{55} is the self-inductance, L_5, of the fifth loop.

$$C_o V_o = C_o E_o - \int\int_0^t dt^2 x_o \qquad V_1 = V_o - L_o x_o$$

$$C_1 V_1 = \int_0^t \int dt^2 (x_o - x_1) \qquad V_2 = V_1 - \sum_{j=1}^{N} M_{j1} x_j$$

$$C_n V_n = \int_0^t \int dt^2 (x_{n-1} - x_n) \qquad (11a) \qquad V_n = V_{n-1} - \sum_{j=1}^{N} M_{j,n-1} x_j \qquad (11b)$$

$$C_N V_N = \int_0^t \int dt^2 (x_{N-1} - x_N) \qquad V_N = V_{N-1} - \sum_{j=1}^{N} M_{j,N-1} x_j$$

$$V_{N+1} = R \int_0^t dt\, x_N \qquad V_{N+1} = V_N - \sum_{j=1}^{N} M_{jN} x_j$$

If we redefine the summations in Eqs. 11b by setting

$$M_{jo} = L_o \delta(j) \qquad (12a)$$

$$M_{on} = 0 \qquad n \neq 0, \qquad (12b)$$

we may write, as a solution to both sets of these equations,

$$\sum_{j=0}^{N} M_{jn}\, x_j = S_n, \tag{13}$$

where

$$S_o = E_o - \frac{1}{C_o}\int\int dt^2(x_o) - \frac{1}{C}\int\int dt^2(x_o - x_1)$$

$$S_n = \frac{1}{C}\int\int dt^2(x_{n-1} - 2x_n + x_{n+1}) \qquad 1 \leq n \leq N-1$$

$$S_N = \frac{1}{C}\int\int dt^2(x_{N-1} - x_N) - R\int dt\, x_N.$$

Note that the appearance of the second forward difference functions of discrete variables is not the result of an approximation, but rather the expression of the discrete physical nature of the interacting elements. Writing Eq. 13 in matrix formalism immediately suggests the solution

$$X = \{M\}^{-1} S, \tag{14}$$

where $\{M\}^{-1}$ is simply the inverse of the inductance matrix.

The generation and inversion of the inductance matrix, and the solution of the N+1 simultaneous equations represented by Eq. 14, was programmed for the IBM 7090 computer. The program will also compute, at selected time intervals, the axial magnetic field at N space points. The numerical solution furnishes a detailed picture of magnetic pulse propagation, the characteristic of greatest interest, and thus we are able, with slight modification, to solve the "equations of motion" for the case in which N closed conducting loops interact with the current-carrying elements of the system. This last solution is beyond the scope of the simple dispersion equation method described above.

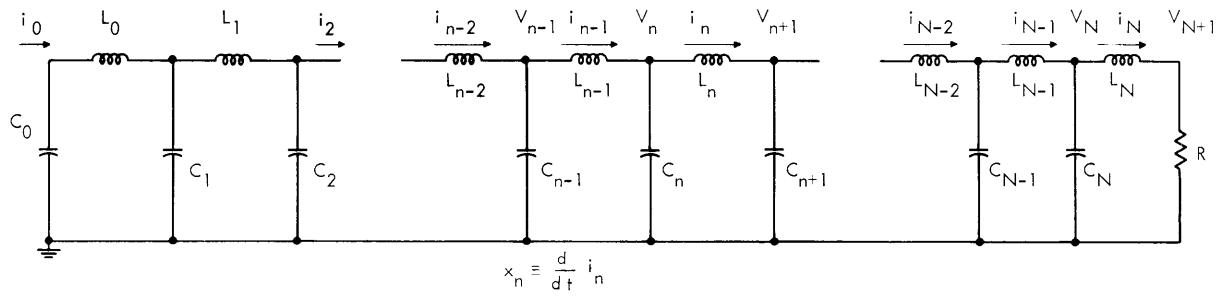

Fig. XI-25. Schematic electrical design and nomenclature for numerical analysis.

3. Accelerator Considerations

The original accelerator design called for as close an approximation as possible to the idealized system of Fig. XI-23. However, the contractor for the ceramic dielectric found it impossible to fabricate the large cylindrical shell called for by that design. The next simpler scheme, build-up of the shell by stacking annular rings, turned out to be, on the basis of experience garnered in the attempted fabrication of the shells, prohibitively expensive. The final design was arrived at as an attempt to utilize very simply constructed ceramic elements. The line is built up of 20 identical sections, each composed of an inner, nearly complete, circular ring, an outer closed circular ring, and 10 dielectric elements connected between the rings (see Fig. XI-26). The capacitors (1.300" × 0.780" × 0.310") are silvered on the two large faces and soft-soldered to the copper rings. This operation must be carried out at 100-120°C ambient temperatures as the ceramic is extremely vulnerable to thermal shock. The ring-capacitor assembly is then placed in a molded silicone rubber (G.E. RTV-20) cup and then vacuum-potted in a silicone-base potting agent (G.E. LTV-610, see Fig. XI-27). This was chosen for its exceptional electrical insulating properties with a dielectric strength in excess of 2 kv/mil in thick sections. The completed "pancakes" are then stacked with the inner tabs connected in such fashion as to form a continuous helix of the inner conductors. Input and terminating sections are added, and the whole assembly pressed into a very tightly fitted cylindrical copper jacket. The outer tabs, connected to the closed rings, are thus forced into contact with the outer jacket which then serves as ground plane for the system. The completed accelerator (with relevant dimensions) is sketched in Fig. XI-28.

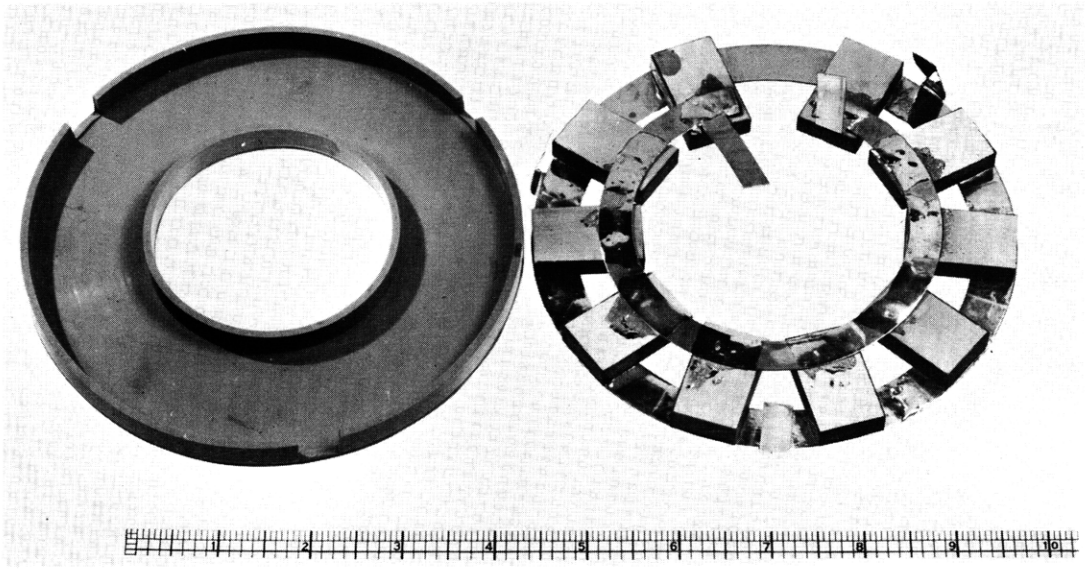

Fig. XI-26. Completed LC circuit before potting.

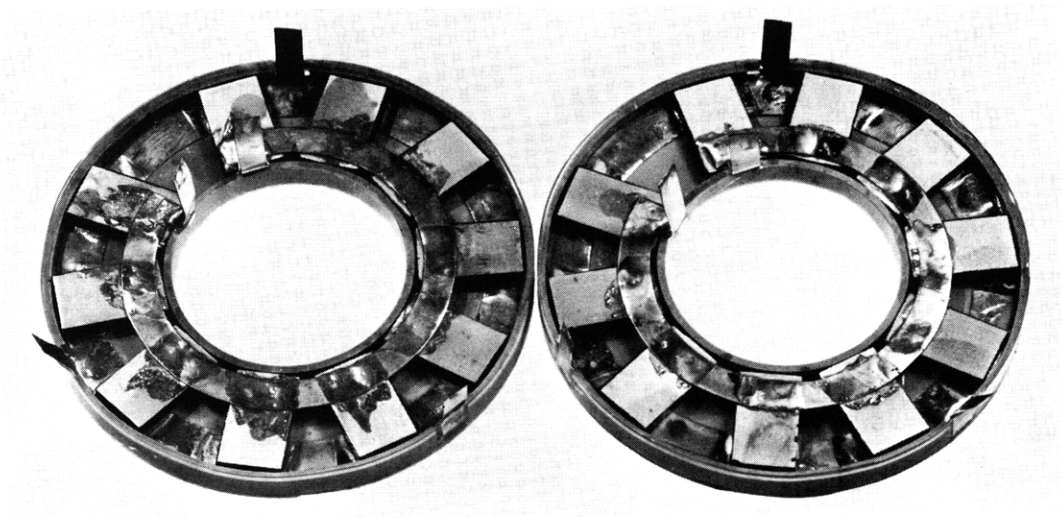

Fig. XI-27. Potted elements. The presence of the very transparent potting agent is just visible in the right-hand photograph of the completed element.

An intensive testing program, both of the dielectric itself and of the completed rings, was carried out before and during construction of the accelerator. The most pertinent result of this study was the observation that although the accelerator does have a moderately high breakdown strength, it is extraordinarily and catastrophically sensitive to rapid voltage reversals of exactly the sort that result from capacitor ringing or transient voltage generation at impedance mismatches. In fact, it was found that properly terminated rings, none of which failed after several hundred 25-kv pulses, failed after only one or two pulses of as low as 6 kv, if an improperly matched terminating resistor was substituted. The termination used on the accelerator was chosen to minimize, as much as possible, all reflections from the end of the line. An identical resistance, connected in shunt across the input terminals serves both to reduce feedpoint mismatch and to effectively decrease the source impedance for any given value of source capacitance.

4. Closed Loops

The design of the individual elements adds a previously unconsidered complication to the behavior of the accelerator. The outer grounded loops are inductively coupled to the inner helix. Indeed, a closed conducting loop has been placed between each pair of inner loops. The gross effect of the closed loops is to reduce the mutual inductance between the inner rings, and at the same time to reduce the effective self-inductance of any single ring. Although this has the happy result of decreasing the impedance of the line and thus promising higher magnetic fields, albeit at a higher propagation velocity, closer inspection reveals that this bright forecast is a snare. The same circulating currents that act to reduce the inductance coefficients also act to reduce the magnetic fields at all points of the system. Analysis of a simple system closely related to the

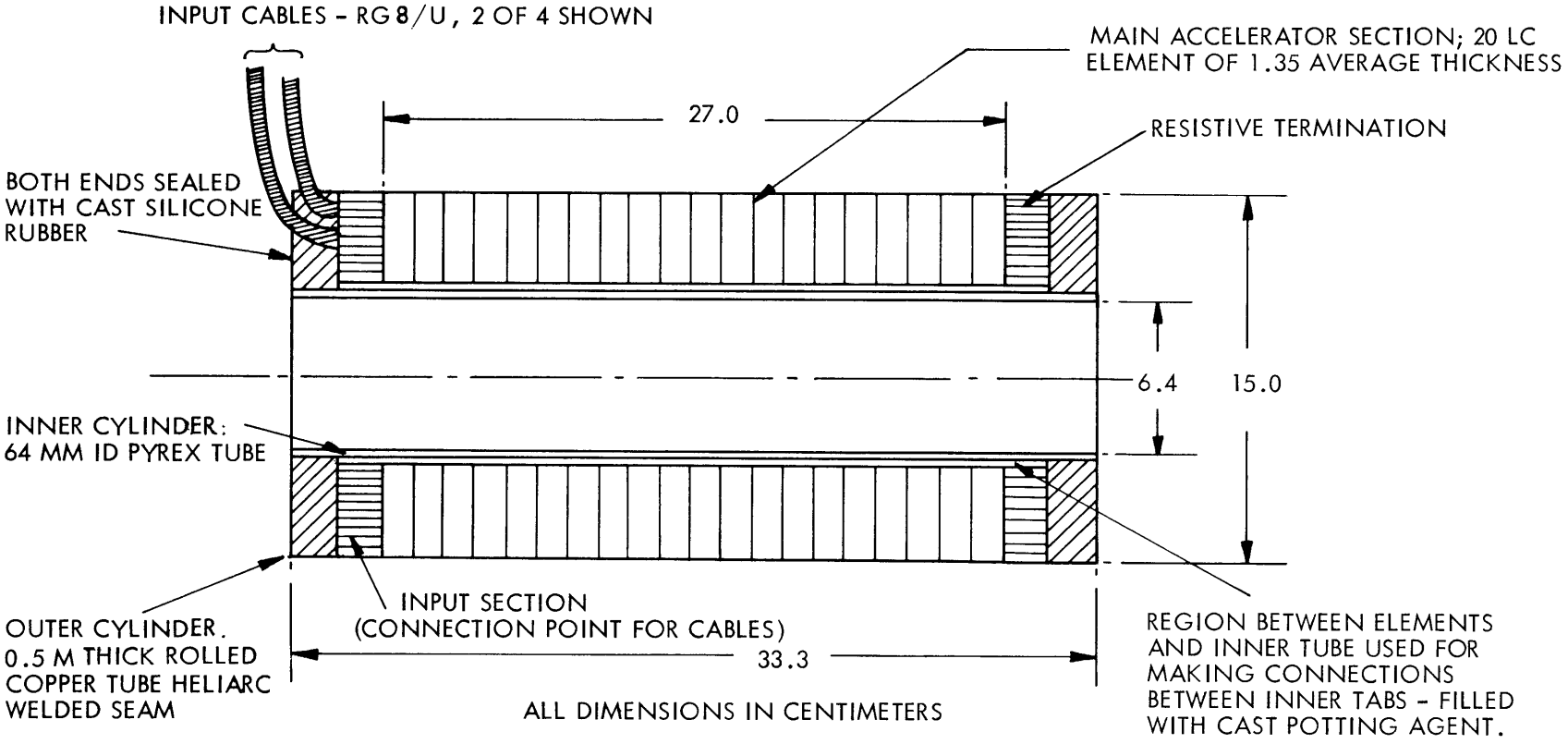

Fig. XI-28. Major dimensions of completed accelerator.

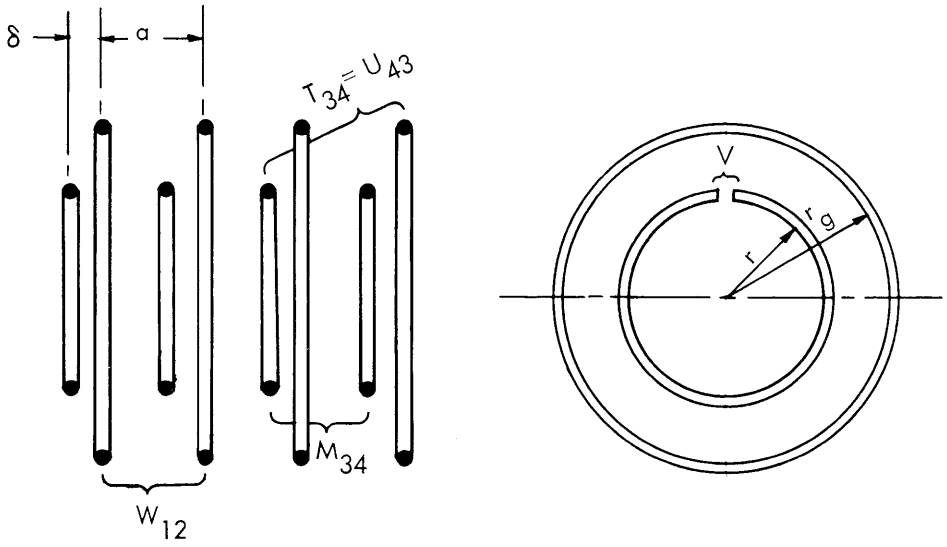

Fig. XI-29. Diagram for consideration of effect of closed inductive loops.

system under discussion shows that the net effect, which must always be detrimental, is a reduction of the peak axial magnetic field by almost 25 per cent.

The effect of the closed loops may be rather simply integrated into the scheme of closed and driven loops depicted in Fig. XI-29. Then, in the same matrix formalism used before, we may write the equation for the voltages on the N driven rings as

$$V = \{M\} X + \{T\} Y, \tag{15}$$

where V_i is the voltage across the i^{th} inner ring, M_{ij} is the mutual inductance of the i^{th} and j^{th} rings, and T_{ij} the same for the outer closed loops. Here X and Y represent the time derivatives of the currents in the inner and outer loops, respectively. In similar fashion, we write the voltage equation for the closed loops

$$0 = \{U\} + \{W\} Y, \tag{16}$$

where $\{U\} = \{T\}^{tr}$, and $\{W\}$ is the inductance matrix for the outer loops. Solution of (15) and (16) yields

$$V = \{M - TW^{-1}U\} X \equiv \{M'\} X. \tag{17}$$

Thus the equations of motion for V are soluble, as before, with the simple replacement of M in Eq. 14 by M' as defined in Eq. 17. Furthermore, the currents in the outer loops may be very simply computed, as the x_c are already in hand, and

$$Y = -\{W^{-1}U\} X.$$

Table XI-3 presents a comparison of some elements of M and M' for the accelerating

Table XI-3. Effect of closed loops on inductance coefficients. (M scaled to units of mμh.)

j	$M_{1,j}$	$M'_{1,j}$	M'/M
1	105.0	84.52	.805
2	73.96	53.33	.721
3	40.89	23.85	.583
4	25.11	12.21	.486
5	16.30	6.84	.420
10	3.09	0.95	.308
20	0.42	0.13	.300

line. Note that the self-inductance, M_{11}, has been reduced by 20 per cent and that the mutual inductance between rings separated by only two intervening sections has been reduced by more than a factor of two. A comparison of the experimental calculations with an experimental measurement of the voltage on the terminating resistor is presented in Fig. XI-30. Even with the large increments chosen for the time integration, the agreement is seen to be quite satisfactory. A complete "run" – voltage, current,

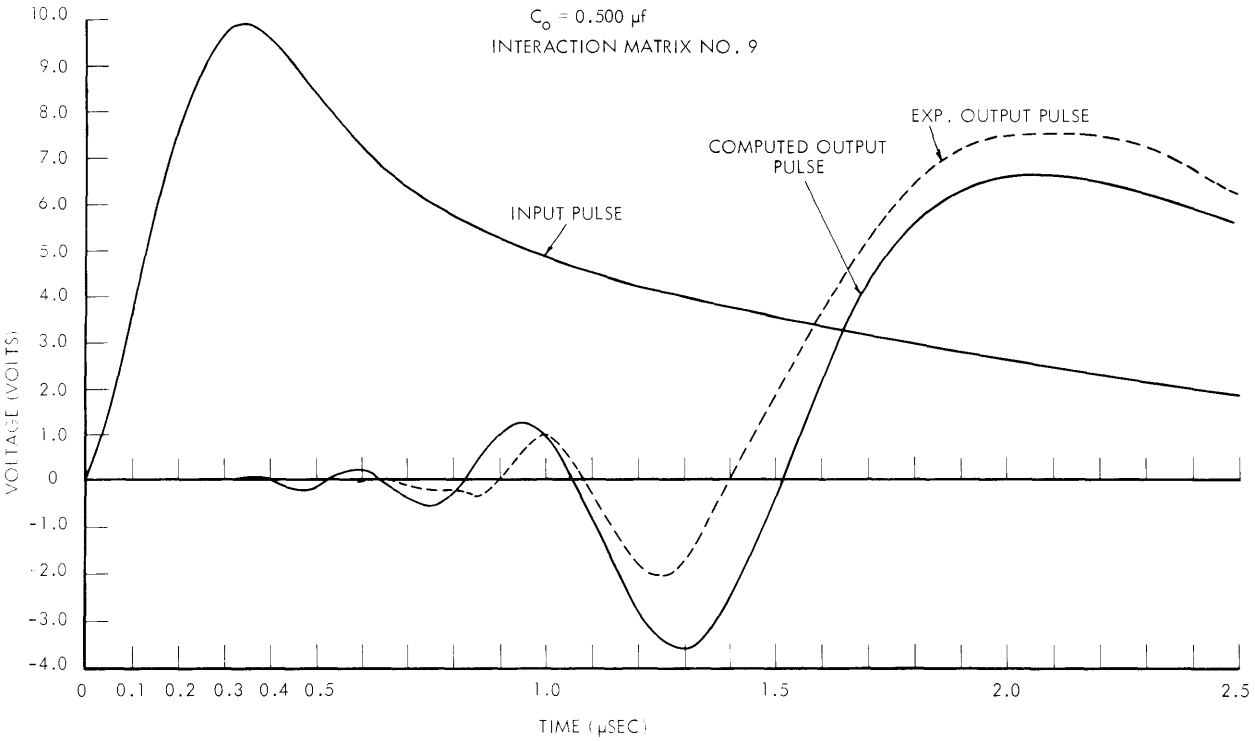

Fig. XI-30. Terminal voltage of completed accelerator.

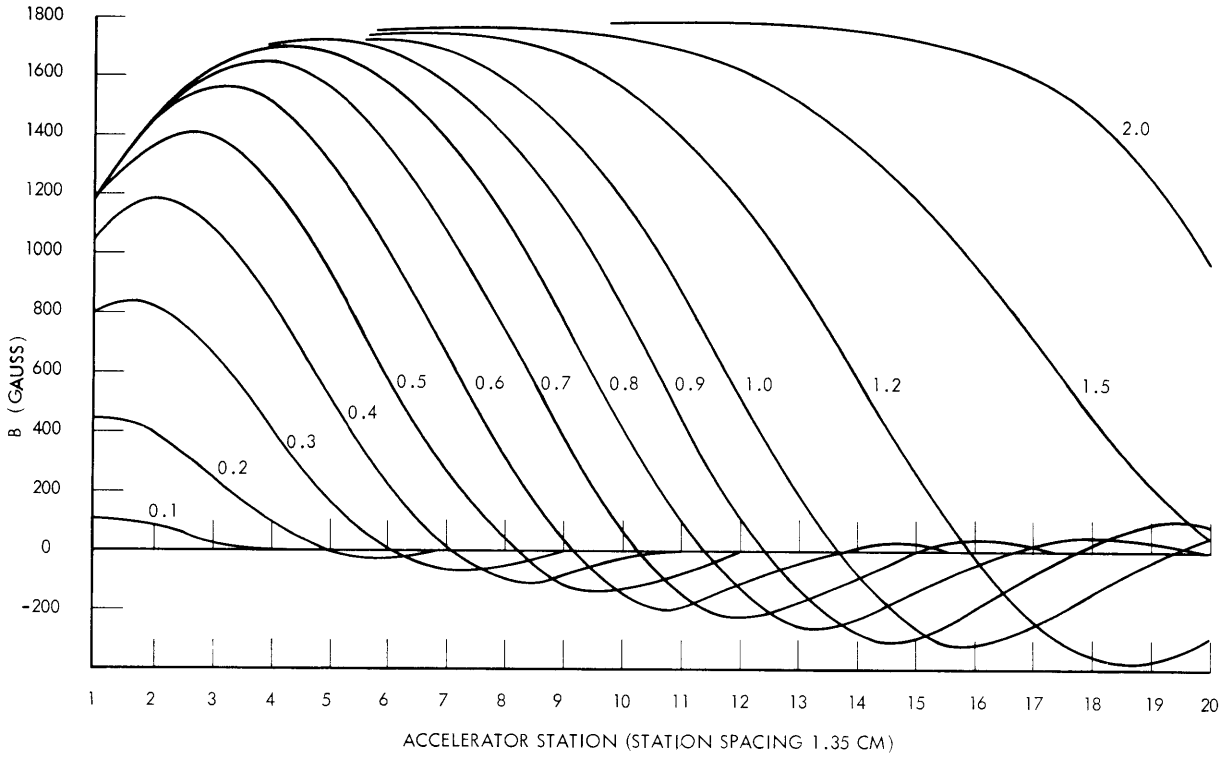

Fig. XI-31. History of magnetic pulse — high driver bank capacity.

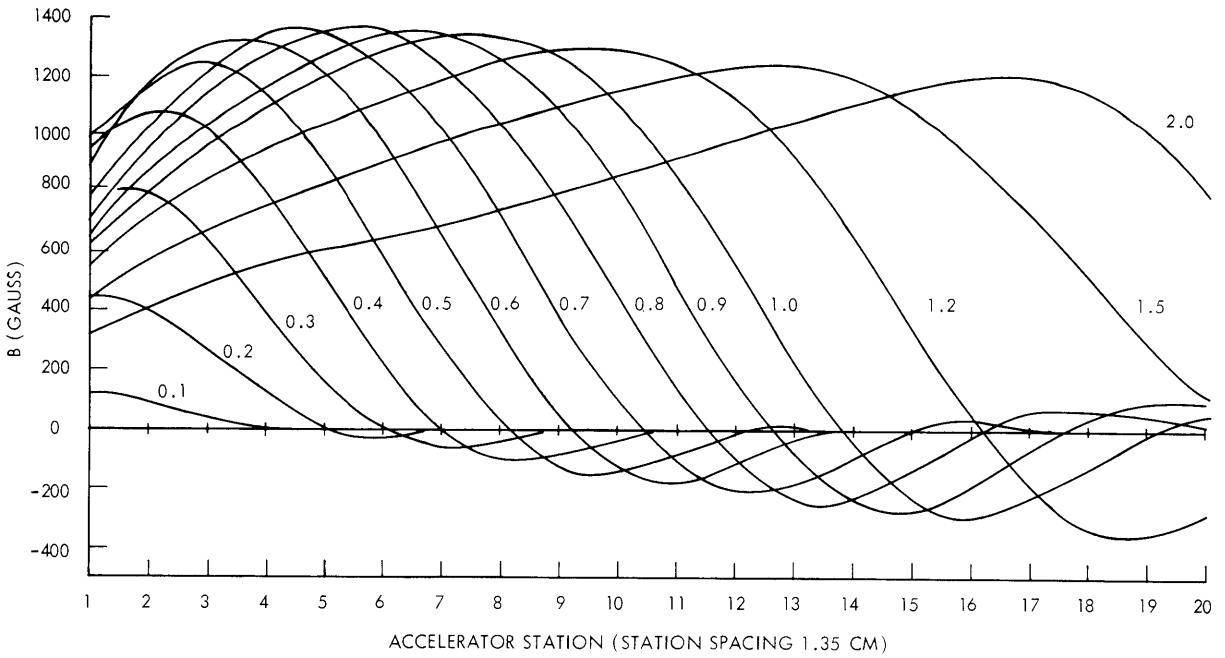

Fig. XI-32. History of magnetic pulse — low driver bank capacity.

magnetic field at 20 space points – takes approximately 4.5 minutes of IBM 7090 time to reach the cutoff value of 2.5 μsec (2500 time intervals). This complexity enforces the use of the largest possible time step.

The computed spatial variation of magnetic field at several instants of time is plotted in Figs. XI-31 and XI-32 for 10 kv initial bank voltage and two values of bank capacitance. The first case, high capacitance, approaches a uniform current distribution at times intermediate between the pulse transit time and the time constant for capacitor voltage decay. That the magnetic field does not also approach that of a long solenoid, i.e., $B|_{ends} = 1/2\ B|_{center}$, is due to the field flattening effect of the closed loops. In any event, most of the input power is wasted, in that any plasma reflection would take place at the crest of the wave and little benefit accrues from the maintenance of a strong field behind the crest. For this reason, and to avoid overheating of the terminating resistors, the low-capacitance system of Fig. XI-32 has been employed in all experiments thus far. The slight loss of peak field is easily compensated by increase of the driving voltage.

5. Apparatus Note

One of the key elements in a high-voltage, high-current system is the main power switch. A rather simple design, based on a suggestion by E. Thompson, has been built and found to operate in exemplary fashion. The switch, a three-element overvolted gap,

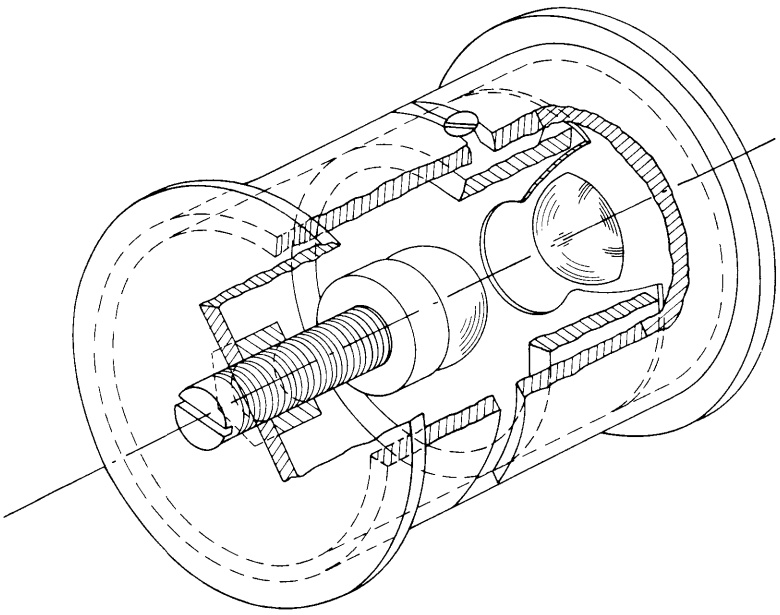

Fig. XI-33. Sketch of three-element spark gap.

is sketched in Fig. XI-33. When driven by a 10-kv positive signal on the trigger electrode, the gap may be adjusted to operate over a series of overlapping ranges between 2-10 kv and 12-30 kv with time delays less than 1 μsec and very small jitter. It has been fired over 5000 times at currents up to 45 kA with no sign of electrode wear.

6. Experimental Results

The interaction of the traveling wave with the hollow-cathode generated plasma is being studied with pendula, photocells, magnetic loops, and electrostatic probes. Preliminary experiments have thus far failed to show the presence of accelerated ions, although there is no doubt that a very strong anadiabatic interaction of some sort is taking place. At the time of the pulse, the light output of the plasma increases by several orders of magnitude, there are large fluctuations in the current and voltage of the arc, and there is evidence that large numbers of electrons are being heated to energies of at least a kilovolt. Results of the more detailed experiments now taking place will be published later.

L. M. Lidsky

References

1. D. J. Rose, L. M. Lidsky, S. D. Rothleder, and S. Yoshikawa, Experimental results on the hollow-cathode discharge, Quarterly Progress Report No. 58, Research Laboratory of Electronics, M.I.T., July 15, 1960, pp. 41-44.

2. L. M. Lidsky, Two meter plasma experiment, Quarterly Progress Report No. 63, Research Laboratory of Electronics, M.I.T., October 15, 1961, pp. 33-40.

3. L. Brillouin, Proc. Symposium on Large-Scale Digital Calculating Machinery (Harvard University Press, Cambridge, Mass., 1948), p. 110.

4. E. Jahnke and F. Emde, Tables of Functions (Dover Publications Inc., New York, 1945), pp. 73-83.